Daniel Filipe Martins de Oliveira

OLEDs em inox: estudos de implementação e degradação

OLEDs on stainless steel: implementation and degradation studies

Daniel Filipe Martins de Oliveira

OLEDs em inox: estudos de implementação e degradação

Dissertação apresentada à Universidade de Aveiro para cumprimento dos requisitos necessários à obtenção do grau de Mestre em Engenharia Física, realizada sob a orientação científica do Doutor Luís Miguel Rino Cerveira da Silva, Professor Auxiliar do Departamento de Física da Universidade de Aveiro.

Este trabalho foi parcialmente financiado pelo projeto QREN - SI ID&T Individual "Desenvolvimento de pastilhas de aço inox electroluminescentes e fotoluminescentes" através dos programas FEDER e COMPETE.

o júri / the jury

presidente / president

Doutora Teresa Maria Fernandes Rodrigues Cabral Monteiro
professora associada com agregação do Departamento de Física da Universidade de Aveiro

vogais / examiners committee

Doutora Isabel Maria das Mercês Ferreira
professora auxiliar do Departamento de Ciências dos Materiais da Faculdade de Ciências e Tecnologia da Universidade Nova de Lisboa

Doutor Luís Miguel Rino Cerveira da Silva
professor Auxiliar do Departamento de Física da Universidade de Aveiro

agradecimentos / acknowledgements

A huge "thank you" to my supervisor, professor Luís Rino, for always believing in me, for all the help, patience, motivation and friendship.
Professor Luiz Pereira for growing all my OLEDs. Over and over.
My closest friends, inland and abroad, for all the moments that kept me motivated.
My parents and sister, for being so patient and raising me properly.
Joana, for being my safe haven.

palavras-chave

oled em inox, estudo de exposição atmosférica, estudo de identidade ótica, barreira flexível, estudo de implementação

resumo

O objetivo deste trabalho consistiu em contribuir para o desenvolvimento de um novo dispositivo, com fins decorativos, baseado num Díodo Emissor de Luz Orgânico (em inglês: OLED) construído sobre um ladrilho de (aço) inox. Este estudo enquadra-se num projecto SI I&DT (Sistema de Incentivos à Investigação e Desenvolvimento Tecnológico) Individual com uma empresa portuguesa da área dos ladrilhos metálicos. O inox possui características óticas particulares que deveriam ser mantidas após a construção do OLED. Um dos principais problemas consiste na transparência ótica, na gama do visível, das várias camadas que constituem o dispositivo. Neste trabalho foram abordados essencialmente dois problemas: o isolamento elétrico da superfície de inox e a eficácia de uma barreira flexível que deverá proteger o OLED da exposição ambiental.

Deste modo, a primeira parte deste trabalho focou-se na avaliação da possibilidade de crescimento de uma camada isolante no ladrilho de inox, espessa o suficiente para aplanar a sua rugosidade mas sem comprometer severamente a sua identidade característica.

A última camada de um OLED é uma barreira protetora que tem como objetivo evitar a exposição ambiental que afecta o tempo de vida do dispositivo. Para esse fim, testou-se uma barreira comercial flexível. Por conseguinte, a segunda parte deste trabalho focou-se no estudo da degradação de um OLED, comparando para isso OLEDs não encapsulados com encapsulados - com vidro (uma barreira de referência) ou com a nova barreira flexível. A comparação baseou-se na evolução temporal do consumo de corrente eléctrica e da electroluminescência do dispositivo. Adicionalmente, utilizaram-se imagens de microscópio para compreender melhor a evolução da degradação. Os resultados sugerem que a degradação dos dispositivos é governada por diferentes processos, quer nos encapsulados ou não encapsulados. No entanto, a barreira encapsulante utilizada permitiu alterar (ou eliminar) os tempos de ativação de alguns desses processos. Estes processos de degradação foram estudados e analisados de forma a permitir uma compreensão mais clara da progressão da degradação que afeta o tempo de vida do OLED tão severamente.

keywords

oled on stainless steel, atmospheric exposition study, optical identity study, flexible barrier, implementation study

abstract

The goal of this work was to contribute to the development of a new device, for decorative purposes, based on an Organic Light-Emitting Diode (OLED) built on top of a stainless steel (StS) tile. The framework of these studies was a SI I&DT (Sistema de Incentivos à Investigação e Desenvolvimento Tecnológico) Individual Project with a Portuguese company in the area of metallic tiles. StS possesses particular optical characteristics that were supposed to be maintained after the OLED was built. One of the major problems is the optical transparency, in the visible range, of the several layers that constitute the device. In this work two particular issues have been addressed: the electric insulation of the StS surface and the effectiveness of a flexible barrier to protect the OLED from environmental exposure.

Therefore, the first part of this work focused on evaluating if an insulating layer could be grown on a StS tile, thick enough to smooth its roughness but without compromising its characteristic identity too severely.

The last layer in an OLED is a protective barrier which aims to avoid ambient exposure that affects the life time of the device. In order to accomplish that, a very thin flexible commercial barrier was tested. Hence the second part of this work focused on studying the OLED degradation by comparing not-encapsulated OLEDs with encapsulated ones - either by glass (a reference barrier) or the new flexible barrier. The comparison was based on the time evolution of the electric current consumption and the electro-luminescence of the device. Plus, microscopy images were used to better understand the evolution of the degradation. Results suggest that different processes rule the degradation of the devices, either encapsulated or not. However, the encapsulation barrier used was able to change (or eliminate) the activation timings of some processes. These degradation processes were studied and analysed in order to accomplish a clear understanding of the degradation's progression that severely affects OLED life time.

Contents

Contents i

List of Figures iii

List of Tables v

1 Introduction 1
1.1 State of the art: OLEDs on stainless steel substrate . . . 2

2 Objectives 3
2.1 Optical Identity Study . . . 3
2.2 Atmospheric Exposition Study . . . 4

3 Theoretical Foundations of Organic LEDs 5
3.1 Introduction . . . 5
3.2 Materials and Energy Bands . . . 5
3.3 Charge Carrier Transport . . . 6
3.4 Single-layer OLED . . . 7
3.5 Multi-layer OLED . . . 8
3.6 Organic Semiconductor - Metal Junction . . . 9
3.6.1 Vacuum Level . . . 9
3.6.2 Energy Alignment at the Interface . . . 9
3.6.3 Band Bending . . . 10
3.7 Degradation Mechanisms . . . 11

4 OLED Growth 15
4.1 Thermal Evaporation . . . 15
4.2 Materials . . . 16

5 Optical Identity Study 19
5.1 Spin-Coating . . . 19
5.1.1 Interference in Thin-films . . . 20
5.2 Roughness and Thickness . . . 21
5.3 Reflectance and Transmittance . . . 23
5.4 Results and analysis . . . 24
5.4.1 Reflectance of the Stainless Steel Tiles . . . 24
5.4.2 Roughness of the Stainless Steel Tiles . . . 25

5.4.3 Thickness of PMMA Thin-films 27
5.4.4 Reflectance of PMMA Thin-films 28
5.5 Conclusions 29

6 Atmospheric Exposition Study **31**
6.1 Encapsulation Methods 31
6.1.1 Transmittance of the Encapsulating Barriers 32
6.2 Construction of the Measurement System 32
6.2.1 Electrical Measurements 34
6.2.2 Optical Measurements 34
6.3 Results and Analysis 34
6.3.1 OLED's Characterization 35
6.3.2 Emission Degradation: Raw Data 37
6.3.3 Emission Degradation: Analysis 39

7 Conclusions and Future Work **45**

Bibliography **47**

List of Figures

1.1 Total OLED display revenue: history and forecast. 1

3.1 π and σ bonds in ethene. Energy levels of a π-conjugated molecule. 6
3.2 Representations of the energy levels of an isolated molecule, a molecular crystal and an amorphous solid. 7
3.3 OLED in equilibrium and non-equilibrium. 8
3.4 OLED schematics. 8
3.5 Electronic structure of an organic-metal junction. 10
3.6 Degradation processes by zone. 11
3.7 (a)Before- and (b)after-crystallization morphology. 12

4.1 Representation of the basic process inside a thermal evaporator. 15
4.2 Representation of the OLED structure used. 16
4.3 Chemical structure of the organic layers used. 16

5.1 Schematic diagram of spin-coating's main steps. 19
5.2 Representation of thin-film interference. 20
5.3 Scheme illustrating PMMA's role. 21
5.4 Representation on how the Dektak calculates R_a. 22
5.5 Illustration of the computational levelling. 22
5.6 Scheme of the tiles' division for reflectance studies. 24
5.7 Average reflectance by zone. 25
5.8 Scheme of the tile's division. 25
5.9 Raw data and fitting for the 5x5 cm polished tile. 26
5.10 Raw data and fitting for the 2x2 cm polished tile. 26
5.11 Raw data and fitting for the 5x5 cm unpolished tile. 26
5.12 Raw data and fitting for the 2x2 cm unpolished tile. 27
5.13 Roughness in zones 1-9 of the four tiles analysed. 27
5.14 Thickness of PMMA as a function of its concentration. 28
5.15 Specular reflectance of PMMA as a function of its concentration. 29

6.1 OLED perspective and encapsulation 31
6.2 Transmittance of glass and flexible barrier. 32
6.3 Diagram representing the trigger line creation process. 33
6.4 Fibre's movement scheme. 34
6.5 I=f(V) and L=f(V) chart for not encapsulated OLEDs. 35
6.6 I=f(V) and L=f(V) chart for encapsulated OLEDs (flexible barrier). 36

6.7 Spectra for t=0s for not encapsulated and encapsulated OLEDs. 37
6.8 Spectral shape over time. 38
6.9 I(t) and L(t) charts. 39
6.10 Dark-spots analysis. 40
6.11 Normalized current and luminance over time. 41
6.12 Normalized luminance as a function of electric current. 41
6.13 Initial 200 s of normalized current and normalized luminance over time. . . . 42

List of Tables

4.1 Typical thickness and energy band values for the OLED grown. 17

5.1 Parameters used for PMMA deposition 20
5.2 Dektak acquisition parameters for stainless steel tiles. 23
5.3 Dektak acquisition parameters for PMMA layers. 23
5.4 Shimadzu UV-2100 specifications. 24
5.5 Parameters of the linear fit. 28

6.1 Ocean Optics acquisition parameters. 34

Chapter 1

Introduction

Around 20% of the electric energy consumed on Earth is for illumination purposes. As an alternative to the traditional incandescent or fluorescent lamps, solid-state light sources (SSLS) are the most promising, offering several advantages such as:

- Environmental and energy saving. SSLS will allow, by 2020, to reduce by 50% the amount of electricity used to illumination, meaning a reduction of 28 millions tons of carbon emitted to the atmosphere every year;
- Higher resistance to vibration and shock;
- Durability;
- Design novelties, if one considers SSLS can be flexible or coupled to flexible materials [1];
- Better monochromatic behaviour [2].

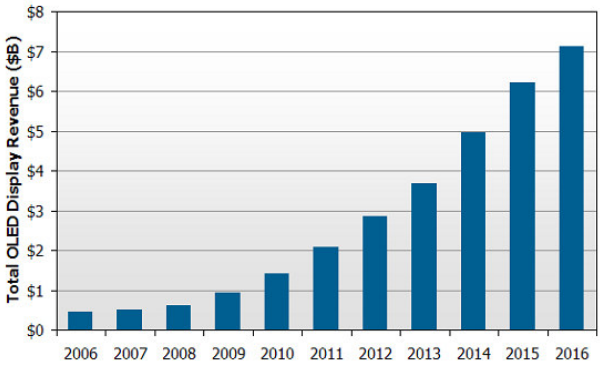

Figure 1.1: Total OLED display revenue: history and forecast [3].

SSLS are divided in two different categories: inorganic, or LEDs (light-emitting diodes), and organic, or OLEDs (organic light-emitting diodes). As alternative for efficient illumination purposes, OLEDs have conventional LEDs as main competitor. One must bear in mind

that LEDs industry has decades of experience and, for that reason, it has its own well established place on the market and offers competitive prices. Nonetheless, OLEDs manage to offer some features that allow them to penetrate in specific market segments, such as decoration. On one hand, LEDs are small, rigid and punctual light sources, requiring an external connection among them to form a line or sheet of light, and the area to dissipate heat is extremely small; on the other hand, OLEDs can be produced as flexible sheets of light with a large area for heat dissipation [4]. OLEDs also offer strong brightness and contrast, a wide-view angle, are predictably a low-cost technology and possess a low density of intrinsic defects by comparison with the inorganic counterparts [5, 6]. Another attraction concerning OLEDs is their durability which, according to predictions, will hit 100 thousand hours; conventional LEDs have 50 thousand, fluorescent lamps have 10-20 thousand and incandescent lamps have one thousand [4].

Let it be noted, however, that even though predictions favour OLEDs greatly, outside of the laboratory one still has to deal with several problems. Even if kept on a shelf an OLED degrades under the attack of oxygen and water. Under electric operation, electrodes and the organic layers degrade even faster. The degradation of these devices will be explained in detail in section 3.7.

1.1 State of the art: OLEDs on stainless steel substrate

The first report on a flat-panel built on a metallic substrate dates back to 1996 [7]. Ever since, the seek of an unbreakable and lightweight substrate has been the motivation of many studies [7, 8, 9, 10, 11].

Nowadays, the market of portable displays is divided in active-matrix liquid crystal displays (AMLCDs) and active-matrix OLEDs (AMOLEDs); both technologies require low-temperature polycrystalline silicon thin-film transistors (TFTs) to operate, being the referred TFTs deposited on glass. Plastic and stainless steel substrates (SSS) present themselves as good alternatives to the traditional glass, each one with its own natural limitations and advantages. As main advantage, plastic substrates offer the possibility to build top- and bottom-emission devices, while opaque metal sheets are limited to a top-emission architecture. Also, metal's roughness needs to be corrected by either a chemical or mechanical polish phase or by applying a smoothing layer. But unlike plastic, SSS are not affected by any length change (shrinkage or elongation) due to gas permeation and are equally more resistant to thermal stress. SSS are also impervious to oxygen and water and offer higher process temperature capability ($\sim 900^{o}$C) [12, 9, 8]. Plus, recent studies suggest that using a metal substrate can improve brightness homogeneity and device's lifetime when compared with glass by improving heat dissipation, since stainless steel has a thermal conductivity sixteen times higher than glass's (typically 16 W/m.K and 1 W/m.K, respectively) [13].

Chapter 2

Objectives

This work is integrated in a SI I&DT (Sistema de Incentivos à Investigação e Desenvolvimento Tecnológico) Individual Project between a Portuguese company and CENTI (Centre for Nanotechnology and Smart Materials), which intends to develop a process to grow OLEDs on stainless steel tiles for decoration purposes. For practical reasons, one has decided to divide the work in two separate parts:

1. Verify if one manages to grow an OLED on a stainless steel tile keeping its optical identity, which will henceforth be referred as *Optical Identity Study*;
2. Study the effects of atmospheric exposition of an OLED, as well as the protection achieved by several encapsulation layers, which will henceforth be referred as *Atmospheric Exposition Study.*

2.1 Optical Identity Study

Regarding the Optical Identity Study, one must consider that all the layers involved in the OLED can contribute to change stainless steel's natural identity. At a starting point, it was assumed that six main layers would be needed: a smoothing/insulating layer, two transparent conducting oxides (TCOs) as electrodes, two organic layers and one encapsulating layer - details on these will be presented during this work. The smoothing layer option overturned the need to use some kind of chemical/mechanical polish, which immediately changes significantly stainless steel's identity; therefore, one has opted to use a layer of poly(methyl methacrylate) - commonly known as PMMA. The following tests were made with the purpose of measuring if and how each layer contributes to the loss of natural identity:

- Roughness of the stainless steel tiles. Only by understanding the typical roughness can one properly decide on the thickness of PMMA to grow;
- Reflectance of the stainless steel tiles without any additional layer on them. This will be compared with optical data of other layers;
- Thickness of the smoothing layer of PMMA;
- Reflectance of the smoothing layer of PMMA;
- Transmittance of the encapsulation layers.

At the end of these tests one should be able to tell accurately how affected the steel's identity is and report such results to the company for their appreciation. Let it be noted that the choice of PMMA for smoothing layer was a result of a bibliographic research for an indicated material, both optically, electrically and mechanically.

2.2 Atmospheric Exposition Study

This part of the work is related to the one described above but not dependant, meaning that either the company likes the final stainless steel identity or not, one shall research for future applications or industrial purposes how effective the barriers are. Therefore, for practical reasons, and considering both glass and stainless steel are good barriers against oxygen and moisture, glass was used as a substrate, aluminium was used as cathode and ITO (Indium Tin Oxide) was used as anode. One shall remind that, in this case, no smoothing layer is needed.

In order to perform this study one developed a system which was able to simultaneously measure optical and electric properties of atmosphere-exposed and encapsulated OLEDs. Details on the system can be found in section 6.2.

Chapter 3

Theoretical Foundations of Organic LEDs

3.1 Introduction

While the origin of the first studies on organic semiconductors dates back to the early 20^{th} century, and even though back in the 1960s electro-luminescence was discovered and the basic processes involved in optical excitation and charge carrier transport were established, only in the 1970s, with the successful synthesis of conjugated polymers and their controlled doping, have the organic materials been used in their first applications [14].

3.2 Materials and Energy Bands

Organic semiconductors can be divided in two major classes: small molecules and conjugated polymers [14].

In common, one can name a conjugated π-electron system formed by the p_z orbitals of sp^2-hybridized carbon atoms. From carbon's four valence electrons, three bond with neighbour atoms and one remains in the p_z orbital; the p_z orbitals of such neighbour atoms overlap, thus forming the π-bonds throughout all the conjugation length. The π-bond electrons have higher mobility than the electrons of σ-bonds since they move freely between atoms due to the orbitals being overlapped. As a consequence of that superposition, the π band splits in two bands: π and π^*. The π band includes the HOMO (Highest Occupied Molecular Orbital), whereas the π^* band includes the LUMO (Lowest Unoccupied Molecular Orbital), and the lowest electronic excitation in conjugated molecules occur in π-π^* transitions, with a typical energy gap of 1.5-3 eV [14, 15].

The major difference between the small molecules and conjugated polymers classes lies on the way they must be processed in order to form thin films: while conjugated polymers need to be processed from solution, making it imperative to use printing techniques such as ink-jet, roll-to-roll or spin-coating, small molecules are deposited by sublimation or evaporation. Some small molecules can also be grown as crystals, allowing intrinsic electronic properties to be studied [14].

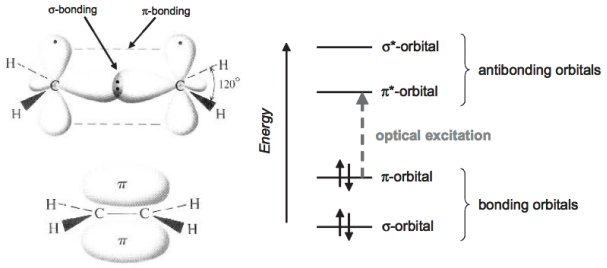

Figure 3.1: On the left: an example of π and σ bonds in ethene. On the right: energy levels of a π-conjugated molecule [14].

3.3 Charge Carrier Transport

In order to understand the transport of charge carriers in organic molecular solids, one must consider it involves ionic molecular states. In other words, if one wishes to create a hole, an electron has to be removed, which will result in the appearance of a radical cation, then allowing the hole to move from one molecule to another. Similarly, electron transport requires negatively charged radicals, or anions. The same principle is qualitatively valid for polymers [14].

Depending on whether one refers to an organized system (such as purified molecular crystals) or a disorganized one (amorphous, like small molecules and most organic emissive layers), the charge carrier transport mechanism differs from band transport to hopping, respectively [1, 14]. Because this work's emissive material lies in the small molecule category, one will focus on the hopping mechanism.

The hopping mechanism consists on providing enough energy to a charge carrier so it can overcome a potential barrier, allowing the carrier to move (or hop) from ion to ion [16]. The cathode work function must be chosen carefully in order to allow the energy difference between itself and the LUMO to be as low as possible, this way preventing losses during the electron injection. By the same principle, anode's work function should match HOMO's energy level to avoid unnecessary losses when holes are being injected [1].

One must bear in mind that electron mobility in organic materials is around one million times smaller than in their inorganic counterparts, like crystalline silicon [1, 16]. Such fact can be explained if one considers that these organic materials are amorphous and therefore the nature of their electronic states is quasi-localized. Plus, their electronic wavefunctions hardly overlap with the wavefunctions of neighbour molecules, rendering charge-hopping much less likely to happen [16]. As a consequence of this property comes the need to use layers in the nanometer range, since they allow low driving voltages but a high electric field and therefore a significant electric current flowing through the device [1].

As stated at the beginning of this section, the transport of charge carriers requires the presence of anions and cations, which can be seen as donors and acceptors. But energy transfer between donor- and acceptor-molecules can happen by the means of intermediate molecules, which are nothing but a bridge between the anion and the cation [17]. To better understand transport in disordered systems one will define the mobility edge ϵ_M, which represents the (energetic) separation between localized and delocalized sites. The localized energy levels available for conduction can be modelled by a Gaussian distribution with a width parameter

σ which is associated with the molecular disorder [14, 18].

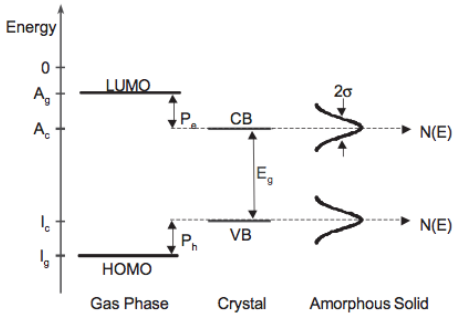

Figure 3.2: From left to right, representations of the energy levels of an isolated molecule, a molecular crystal and an amorphous solid [14].

Electrons above ϵ_M contribute to band transport, while those near it ($\sim kT$) are eligible to be thermally ionized into delocalized states. Nonetheless, current can still be carried if one goes deeper into the localized density of states, whether by hopping or by thermally activated tunnelling. These sites are often referred to as shallow traps, while deep traps are too deep to be thermally activated and therefore are considered static [19].

3.4 Single-layer OLED

Single-layer OLEDs are not commonly used nowadays due to their lack of efficiency, considering the cathode-LUMO and anode-HOMO gaps are usually high (meaning the energy difference between them is high). Between the anode and the cathode one finds only the active layer - the one responsible for light emission. When one applies a potential to the device, the electrons hop from the cathode to the LUMO and the holes jump from the anode to the HOMO. Eventually, some charge carriers with opposite charge signal will bond and form excitons; when such excitons relax they radiate with a certain frequency which depends of the layer one is using [20]. The frequency is dictated by Planck-Einstein equation

$$E_{electron} + E_{hole} - E_{recombination} = \frac{hc}{\lambda} \tag{3.1}$$

where the frequency $f = \frac{c}{\lambda}$ and the emitted energy consists on the sum of the excitation energy minus the energy used for the recombination, as it is mathematically written in equation 3.1[21].

When an OLED is in thermal equilibrium, without any external field applied to it, the energy levels can be represented as figure 3.3a shows.

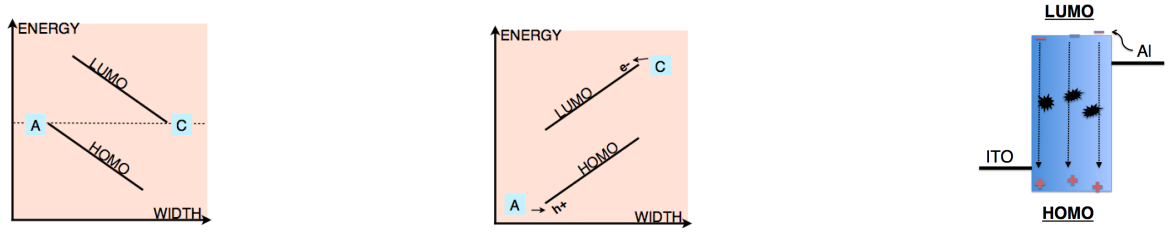

(a) OLED in equilibrium

(b) OLED with external field applied

(c) Energy diagram.

Figure 3.3: (a),(b) OLED in equilibrium and non-equilibrium adapted from [1], where A, C stand for anode and cathode, respectively. (c) Energy diagram for a single-layer OLED adapted from [22].

As one can learn from the same figure, the anode and the cathode are naturally at the same potential, and because Fermi's level is in equilibrium between the electrodes, no current flows through the device. For it to happen, one must apply a potential to the organic layer greater than its own. The oblique lines intend to show that neither the HOMO nor the LUMO energies are constant throughout the OLED [1]. If one overcomes the built-in potential of the organic layer with a greater, external one, then the image 3.3b is valid instead of image 3.3a. Let it be noted that, in this case, electrons (e-) and holes (h+) flow to the LUMO and HOMO, respectively.

3.5 Multi-layer OLED

The basic principle of a multi-layer OLED is the same one described in the previous section. However, as the name suggests, several layers are used between the electrodes instead of just one, to enable a more efficient hopping by lowering the energetic barriers at the interfaces, thus allowing more efficient emission. The simpler example of a multi-layer OLED is the one where only two layers are used: the hole transport layer (HTL - with a high hole mobility,) and one that is both the electron transport layer (ETL - with a high electron mobility) and the emissive layer (EML) [14], as one shows in figure 3.4a.

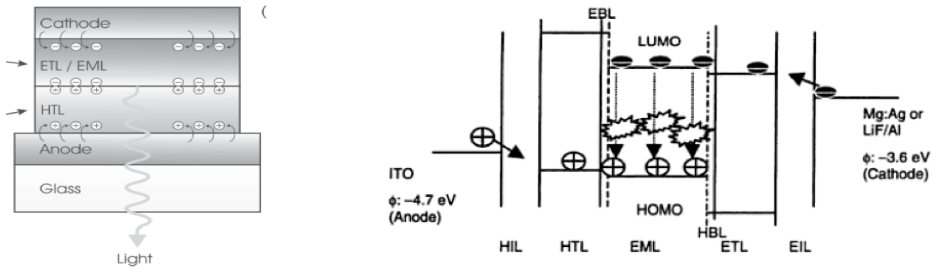

(a) Two-layer OLED [14].

(b) Five-layer OLED [20].

Figure 3.4: Schemes of two-layer and five-layer OLEDs.

But nowadays high-efficiency and durable OLEDs consist of four, five or more layers. Besides HTL, ETL and EML (ETL and EML can be two different layers, as opposed two what was described above), one can add electron and hole injection layers (EIL and HIL, respectively), whose function is to decrease the cathode-ETL and anode-HTL potential barriers. This way one can ensure an abundant charge carrier injection [20, 23]. To illustrate what occurs, a diagram is shown in image 3.4b.

One must emphasize that HTL and ETL work as barriers for electrons and holes, respectively, originating a high density area of charge carriers (the EML), favouring recombination and, as a consequence, the general efficiency of the OLED. Image 3.4b shows the referred barriers in dashed lines, signed as EBL (electron blocking layer) and HBL (hole blocking layer) [24, 23].

3.6 Organic Semiconductor - Metal Junction

Since the cathodes are commonly metals, that implies a junction between them and the adjacent organic layer. Interesting and important processes happen in that interface, which shall be described in this section.

3.6.1 Vacuum Level

Before starting any description concerning the physical principles of a junction between an organic semiconductor and a metal, one must clarify the definition of vacuum level (VL) at infinite distance and near a surface. VL at infinite distance, or VL(∞), is the energy of an electron at rest in vacuum. This value is often considered an invariant energy reference. On the other hand, VL near a surface, or VL(s), corresponds to the energy of an electron at rest outside a solid but close enough to be under its potential. VL(s) is used in the measurement of ionization energy (I), electron affinity (A) and work function (Φ); therefore, for organic-metal contact, the VL used must be VL(s) instead of VL(∞) [25]. Details on this will be explained below.

3.6.2 Energy Alignment at the Interface

In figure 3.5a one can identify the electronic structure of a metal and an organic semiconductor at a distance which be considered infinite. Figure 3.5b, on the other hand, represents the situation of contact between both surfaces, as the organic structure shifted position and moved inside a zone where the electric field of the metal is significant. Figure 3.5c is a schematic representation of 3.5b assuming a common VL(s) in all zones, represented just as VL in the diagram. Consequently, the energy in the neighbourhood of the organic compound is no longer VL(∞) but is now VL(s) instead. Φ_m, Φ, Φ_B^n, Φ_B^p, E_F stand for work function of the metal, work function of the organic, electron- and hole-injection barrier and Fermi level, respectively. Other symbols are described in the previous section. Finally, figure 3.5d represents the interface with a Δ shift of VL, caused by a dipole layer formation. Several factors such as charge transfer across the interface, rearrangement of the electron cloud or inter-facial chemical reaction, among others, contribute to this dipole, and the value of Δ depends on how strong the dipole is [25].

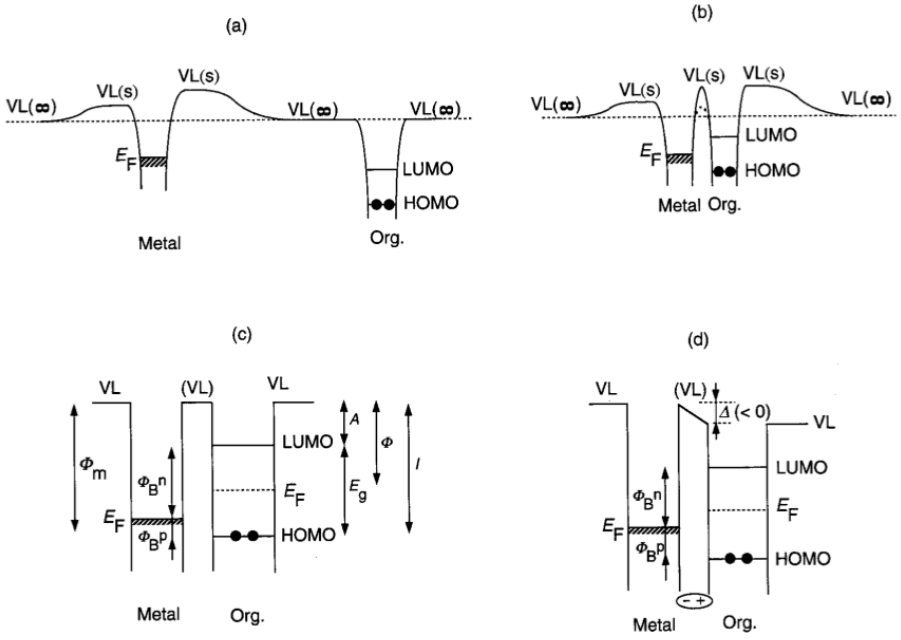

Figure 3.5: Electronic structure of an organic-metal junction in the following situations: (a)distance which be considered infinite; (b)situation of contact; (c)representation of *(b)* assuming VL(s)=constant=VL; (d)Δ shift of VL caused by a dipole [25].

3.6.3 Band Bending

Band bending must be considered whenever one deals with a thick organic layer. The reason behind band bending is that the interfaces shown in 3.5c and 3.5d are not in electrical equilibrium, which would mean the Fermi levels to be at the same energy. This lack of equilibrium happens because the metal and the organic layer usually have different work functions; as a result, electron flow and redistribution of charge carriers in the organic layer will happen until the Fermi levels align, provided there is a sufficiently large number of charge carriers available [25].

During the redistribution of charges, Poisson equation governs the potential distribution at the interface. Consequently, in order to align Fermi levels, a diffusion layer with the resultant band bending appears.

By bringing two surfaces into contact, one is actually starting a thermodynamic process, which will aim at achieving equilibrium by means of a charge flow across the interface. Such flow will equalize the potentials of the two materials in contact. As a result, band bending or interface dipoles will appear at one's system. If one assumes the interaction is not chemical, energy shifts will depend on either the work function and the charge carrier densities of both materials [14].

3.7 Degradation Mechanisms

An OLED's lifetime is severely affected when it is exposed to oxygen and water vapour, the two major external degradation factors. However, those effects are strongly reduced if one is able to produce an OLED in a controlled environment. Typical layer-by-layer and interface-by-interface degradation is presented and summarized below in a picture presented by Junji Kido, a reference in the OLED field. A general description of each degradation mechanism is presented.

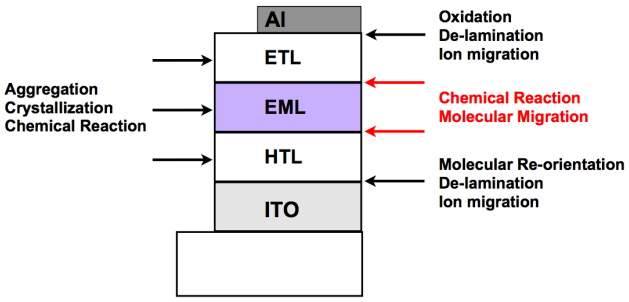

Figure 3.6: Degradation processes by zone for a typical three-layer OLED [26].

Starting for typical electrode degradation, one can immediately refer that the cathode, given its role of injecting electrons into the emissive layer, is usually a metal with a low work function. So it is naturally very reactive, characteristic which becomes a problem if that cathode is exposed to oxygen or moisture: most likely the metal will oxidise, but water vapour and oxygen can also penetrate to the interface between the cathode and the organic adjacent to it. This will increase the resistance and therefore require a larger current density to achieve light emission. On the other hand, the anode's function is to inject holes into the emissive layer. A high concentration of oxygen on the anode will create a negatively charged surface layer between the anode and the organic layer adjacent to it. This happens because oxygen is electro-negative and such effect causes a high hole concentration at the interface between the anode and the nearest organic layer [27].

Regarding ion migration, one knows that ionic diffusion consists on ions from the electrodes migrating into the EML (through ETL in image 3.6). Such ions are responsible for the appearance of fluorescence quenchers, which are responsible for a luminance decrease under a constant driving current. Besides, the moving ions create a built-in voltage that raises the driving voltage for a fixed electrical current; in other words, they induce an internal field which partially cancels the external one [28, 29]. On the other hand, there is the unstable cation model, which consists on the following: the heterojunction of an OLED has the purpose of confining the carriers and therefore increasing the efficiency. However, this piles up carriers at the HTL-EML interface, and since holes injected from the HTL to the EML form chemically unstable cations in the EML, this will speed up the appearance of nonradiative trapping centres. The result is decay in luminance and an increase of the driving voltage of the device [28].

Delamination, which takes place mostly in the cathode, usually happens when there is diffusion of moisture through pin-holes - defects that often appear when there are pre-existing particles on the substrate where the metal thin film (cathode) is grown. Consequently, those sites normally appear as dark-spots (nonemissive regions) [30].

Chemical reactions are also a major degradation concern and are, in part, directly linked to the need of an encapsulating barrier. New, undesirable chemical species are produced when water and oxygen come into contact with the organic layers. This leads to a removal of emissive species, resulting in an immediate luminance decrease [31]. Specifically in small-molecule

OLEDs, molecular migration has also to be considered. One shall remind that, in organic semiconductors, electrons hop from molecule to molecule. This makes molecules negatively charged for some time, thus being driven by the bias towards the ITO anode if the device is operated under direct driving voltage [32]. Another molecular-related degradation factor, even though experiments suggest it is reversible, is the reorientation of molecular dipoles. According to D. Zou, T. Yamada and their team, who have extensive research published in the area, spontaneous and reverse-bias recovery are reported [33, 34, 35].

Aggregation is referred by Kido et all [26] as a process that can happen in all organic layers. It happens due to high molecular concentration within thin-films [36], leading to the appearance of mono-crystals, which originate trap sites for electrons and/or excited states, and therefore to a decrease in the device function properties [37]. Crystallization of organic materials has also to be accounted for device degradation. It heavily affects materials with low glass transition temperature [31]. The grown crystals are most of the times thicker than the film that originated them, affecting adjacent layers [38, 39]. Some of the materials used in one's OLED are reported to frequently suffer from crystallization, mainly NPB and Alq_3 (details on these can be found in section 4.2).

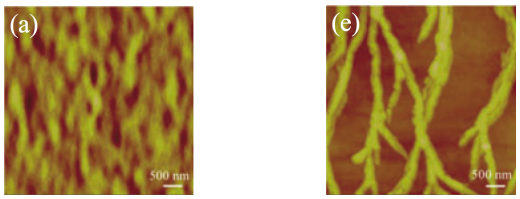

(a) Amorphous. (b) Crystallized.

Figure 3.7: (a)Before- and (b)after-crystallization morphology [39].

In fact, it was this very property which was behind the choice of such materials to this work. By using them, one can study how each barrier blocks (or not) the degradation processes without having to wait hundreds of hours, as it happens in other materials.

Until now, one has merely made a description of the processes involved in OLEDs' degradation. However, it is important to introduce mathematical models that might explain how OLEDs degrade, which is what will follow.

In an ohmic contact, assuming low voltages and not considering diffusion, the current density in a device can be written as:

$$J_{ohm} = eN_0\mu\frac{V}{L} \tag{3.2}$$

where e, N_0, μ, V and L stand for electron charge, number of free electrons per unit volume, electron mobility, voltage applied and sample thickness, respectively [40, 41]. But as tension rises, the electrons injected from the electrode outnumber the ones that were initially in the semiconductor. This is called the space-charge-limited (SCL) regime, and the equation that governs the current density becomes:

$$J_{scl} = \frac{9}{8}\varepsilon_r\varepsilon_0\mu\frac{V^2}{L^3} \tag{3.3}$$

where ε_r and ε_0 stand for the dielectric constant and permittivity in vacuum, respectively [40, 42]. It is intuitive to identify μ as the responsible for the decrease in the electric current,

considering the nature of the other elements of the equation.

As explained in this section, crystallization is a major mechanism of degradation. Since it is directly related to temperature increment, it is an obvious deduction to state temperature increases during device operation. So it becomes of interest to describe the dependence of μ with temperature T, particularly for Alq_3, which is a modified Poole-Frenckel law [41]:

$$\mu(F,T) = \mu_0 \exp\left(-\frac{\Delta E - \beta_{PF}\sqrt{F}}{k_B T_{eff}}\right) \tag{3.4}$$

where F stands for the electric field and is given by:

$$F = \frac{V - V_{bi}}{d} \tag{3.5}$$

The Poole-Frenckel factor and T_{eff} are defined as:

$$\beta_{PF} = \sqrt{e^3/(\pi\varepsilon_r\varepsilon_0)} \tag{3.6}$$

$$\frac{1}{T_{eff}} = \frac{1}{T} - \frac{1}{T_0} \tag{3.7}$$

In equations 3.4 and 3.7, ΔE stands for the activation energy when F=0, T is the temperature, T_0 is an empirical parameter and k_B is the Boltzmann's constant [41]. Looking at equations 3.3 and 3.4, it becomes clear that

$$\mu \propto \exp\left(\frac{1}{T}\right) \Rightarrow J_{scl} \propto \exp\left(\frac{1}{T}\right) \tag{3.8}$$

Alq_3 carrier mobility also depends on air exposure, according to several reports. If it is exposed to oxygen and mainly water, the corresponding mobility decreases [43, 44]. According to equation 3.3, this has the direct consequence of decreasing the value of the electric current flowing through the device.

It is then of interest to reveal one more relation, which is the current density of a Schottky thermionic emission:

$$J_S = AT^2 \exp\left(-\frac{\Phi_B + \sqrt{\frac{e^3 F}{4\pi\epsilon_0}}}{k_B T}\right) \tag{3.9}$$

where A stands for the Richardson constant, T is the temperature and Φ_B is the injection barrier height [45]; all the other parameters have already been defined in this section. From the previous relation one can immediately tell that $J \propto T^2 \exp(-\Phi_B)$, thus giving Φ_B a major role in OLED degradation. According to Ta-Ya Chu et al [45], two main reasons for a Φ_B rise are offered: migration of metallic ions to the organic layers and/or oxidation of the organic/metal interface.

Chapter 4

OLED Growth

4.1 Thermal Evaporation

Thin film deposition methods are divided in two major classes: Chemical Vapour Deposition (CVD) and Physical Vapour Deposition (PVD). The last can be divided in two categories: sputtering and thermal/vacuum evaporation, being thermal evaporation the technique used during this work and therefore is the technique one shall focus on.

If one desires to evaporate a material in vacuum, one manages to do so if the temperature of a material is increased until the correspondent vapour pressure matches or surpasses the existing atmospheric pressure. From that point on, the material's atoms at its surface abandon it and move to a surface where they can adhere to or condense. The vacuum depends on the material one is evaporating and can typically range from 10^{-4} mbar to 10^{-8} mbar. The heating method used was resistive heating (electron beam heating can also be used), which consists on a high current flowing through a crucible which is also a holder for the material one wishes to evaporate. If one considers the vacuum level it is easy to infer that the atoms travel with no resistance until a surface is found, and the kinetic energy they gain during their route is enough to guarantee a good adhesion to the substrate where one wishes to deposit the film [46, 47].

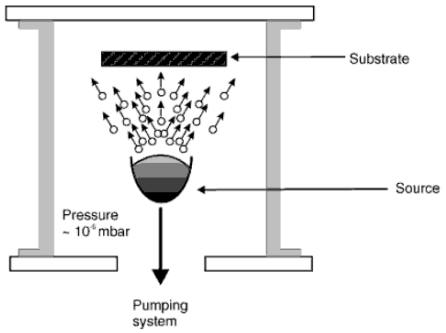

Figure 4.1: Representation of the basic process inside a thermal evaporator [48].

4.2 Materials

The device grown to process the necessary studies was a three-layer OLED, with Aluminium used as cathode and ITO as anode. The three layers used were N,N'-diphenyl-N,N'-bis(1-naphthyl)(1,1'-biphenyl)-4,4'-diamine (NPB) mixed with 1% rubrene / 2,9-dimethyl-4,7-diphenyl- 1,10-phenanthroline (BCP) / 8-Hydroxyquinoline aluminum (Alq3), thus the final configuration ITO / NPB+1%Ru / BCP / Alq3 / Al as shown in figure 4.2.

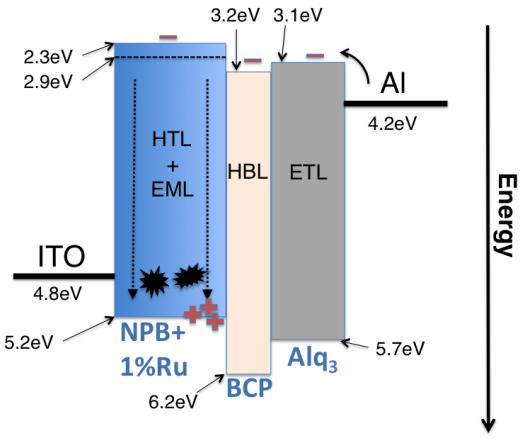

Figure 4.2: Representation of the structure used, as well as energy levels and barrier functions.

As one can see from the picture, ITO provides holes to the HTL/EML and Aluminium provides electrons to the ETL. Recombination is favoured in NPB+Ru layer since holes find in the BCP layer a high energy barrier to overcome (check table 4.1 for details). Is it important to stress that Rubrene's energy bands appear inside NPB's, since the mix between the two materials is a physical one and not a chemical one.

One shall now present the chemical structure from the presented organic layers, as well as the thickness of each.

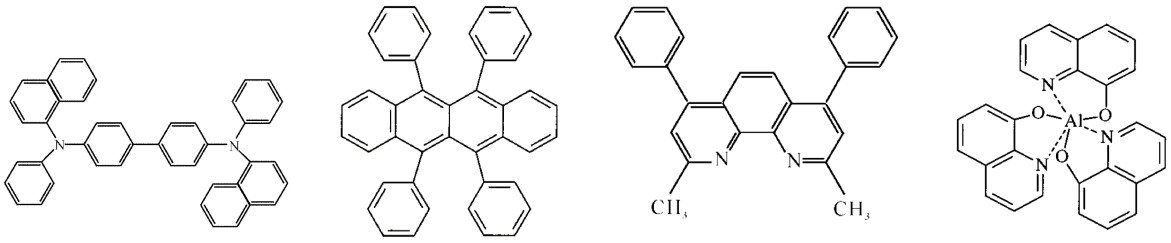

(a) NPB [49] (b) Rubrene [29] (c) BCP [49] (d) Alq3 [29]

Figure 4.3: Chemical structure of the organic layers used.

The table below presents the thickness of each constituent layer of the OLED - values provided by Professor Luiz Pereira. It also presents the typical values of HOMO and LUMO energies (they differ slightly in the literature) according to [49].

Table 4.1: Typical thickness and energy band values for the OLED grown.

-	NPB	Rubrene	BCP	Alq3
Thickness /nm	50		10	30
HOMO /eV	5.2	5.2	6.2	5.7
LUMO /eV	2.3	2.9	3.2	3.1

One shall stress that, as explained in figure 4.2, NPB and Rubrene form one singler layer, reason why in the table above there is only one value for their thickness.

Chapter 5

Optical Identity Study

In this chapter one will introduce physical principles useful to describe the processes involved in the Optical Indentity Study. One shall also describe the processes and the reason they have been used.

5.1 Spin-Coating

Spin-coating is a widely used technique by the microelectronics industry to deposit polymers. It consists on applying a quantity of fluid on the vacuum-held substrate followed by a stage where the substrate is spun (rotated), typically at several thousand revolutions per minute. The solution will then flow radially outwards, reducing the fluid's thickness. The last stage is to evaporate the solvent, leaving a uniform thin-film on the substrate [48].

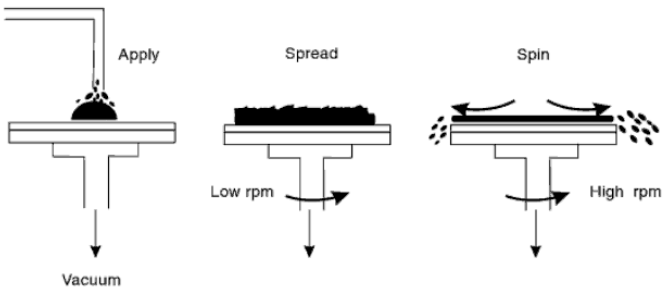

Figure 5.1: Schematic diagram of spin-coating's main steps [48]

One of the simplest theories that governs the process is expressed in equation 5.1 and relates the final thickness of the film, d, with the viscosity coefficient and density of the solution used, η and ρ respectively, the spinning time, t, and the angular speed one used, ω [48].

$$d = \left(\frac{\eta}{4\pi\rho\omega^2}\right)^{\frac{1}{2}} .t^{-\frac{1}{2}} \tag{5.1}$$

One used spin-coating to produce the smoothing layer of PMMA over the stainless steel tiles. Several concentrations (w/w) of PMMA on chloroform solvent were tested, between

1-5%. The parameters used were those listed in table 5.1.

Table 5.1: Parameters used for PMMA deposition

Speed /rpm	Spin Time /s	Oven Time /min	Oven Temperature /^{o}C
1500	30	30	60

5.1.1 Interference in Thin-films

The kind of optical analysis described in this work often leads to observing a pattern due to interference phenomena. As such, a short description of the principles will be made.

Lets start by considering a film of thickness d and refractive index n_i. When a beam of light falls on the top surface of the film with an angle θ_1, part of it is reflected and part of it is transmitted. When the transmitted wavetrain reaches the bottom of the film the process repeats: part of the beam is transmitted and part is reflected; this new angle shall be called θ_2, the angle of refraction. At this moment there are two reflected and two transmitted beams, which will lead to interference [50, 51].

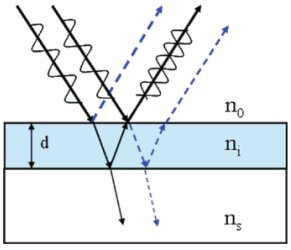

Figure 5.2: Representation of thin-film interference [50].

Focusing on the reflected beams, since in one's case the substrate is opaque, the math that governs the process is the following [51]:

$$\Delta = 2n_i d\cos\theta_2 + \frac{\lambda}{2} \tag{5.2}$$

Δ represents the path difference between the two reflected beams. The *maxima* of interference happens for a path difference of

$$\Delta = k\lambda \tag{5.3}$$

whereas the *minima* happens for the cases when the difference is

$$\Delta = \left(k - \frac{1}{2}\right)\lambda \tag{5.4}$$

with k being the order of interference. So one can write the conditions for *maxima* and *minima* of interference like:

$$2n_i d\cos\theta_2 + \frac{\lambda}{2} = k\lambda \tag{5.5}$$

$$2n_i d\cos\theta_2 + \frac{\lambda}{2} = \left(k - \frac{1}{2}\right)\lambda \tag{5.6}$$

In this work's context, refractive indexes n_0, n_i, n_s refer to air, PMMA and stainless steel, respectively, where d is the thickness of the PMMA smoothing layer.

5.2 Roughness and Thickness

During this work, it was necessary to measure the roughness of stainless steel tiless to decide which should be PMMA's thickness to deposit over it. PMMA played two essential roles: to act as a surface smoother and as an electrical insulator - the electrical resistivity of the steel used is 7.3x10^{-1} Ω.mm^2/m and PMMA's is 1x10^{19} Ω.mm^2/m [52, 53]. One one hand, the surface on which one wishes to grow the OLED cannot have a high roughness to guarantee the homogeneity of the TCO layer and prevent any electric shorts. On the other hand, one needs to insulate the OLED electric flow from the stainless steel tile, which is a conductor itself. By looking at image 5.3 (not at a real scale) one can visualize PMMA's role in the process.

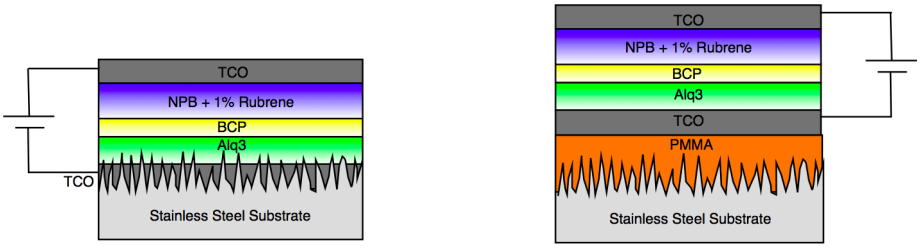

(a) OLED without PMMA layer.

(b) OLED with PMMA layer.

Figure 5.3: Scheme illustrating PMMA's role.

It is easy to understand that PMMA's thickness must be higher than the roughness of the tiles if one wants it to be a good insulator and surface smoother.

For roughness and thickness measurements a Dektak 150 from VEECO was used. The Dektak 150 acquires data electro-mechanically by moving the sample beneath a diamond-tipped stylus. When a 2-axis stage moves the sample, the stylus is moved vertically by morphology changes of the sample, thus producing an electric signal proportional to the stylus translation. Length, speed and stylus force can be manipulated by the operator using a computer interface [54].

The most widely used parameter of roughness is the Ra, or average roughness [54]. It consists on the arithmetic average deviation from the mean line, and is expressed mathematically by:

$$R_a = \frac{1}{L}\int_{x=0}^{x=L} |y|dx \tag{5.7}$$

where L is the assessment length, y is the height under/over the mean line and $0 < x < L$.

Sometimes it is also useful to use Rq, or root-mean-square of the roughness [54]. Rq's

interest is greater in optical analysis, as it is directly related to the optical quality of a surface (which is what one wants to evaluate in the end). Is is expressed by:

$$R_q = \sqrt{\frac{1}{L}\int_0^L y^2(x)dx} \tag{5.8}$$

These direct values given by the equipment can be misleading, though. If one looks at the chart in figure 5.4 one immediately understands that the horizontal mean line clearly

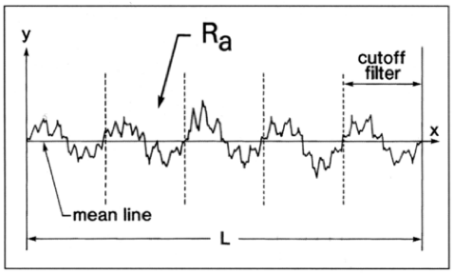

Figure 5.4: Representation on how the Dektak calculates R_a [54].

indicates the system assumes the substrate is plain. However, since our tiles result from common industrial production and not a carefully laboratory one, they do not necessarily possess that configuration. What is visible to the naked eye is that some are convex, and thus the Dektak system would not be able to compensate such property. Plus, the fact the mean line is horizontal, or $y(0) = y(L)$, means an assumption of horizontality from the sample. However, this is invalid in our system. What one has stated was that $y(0) \neq y(L)$, since the edges of the tile were bent using industrial hardware, leaving the waver uneven.

In order to calculate an appropriate parameter that characterizes the roughness according to this work's needs, one has decided to develop a script in $MatLab^{®}$ which was able to:

1. Force $y(0) = y(L)$. By linking $y(0)$ to $y(L)$ one calculated a slope m. Using that slope, and the values of x acquired by the Dektak 150, one calculated the value of y using the trivial equation $y = mx + b$ for a line. One has then subtracted that value of y to the value of y retrieved by the Dektak 150. Figure 5.5 shows the difference between before and post-processing;

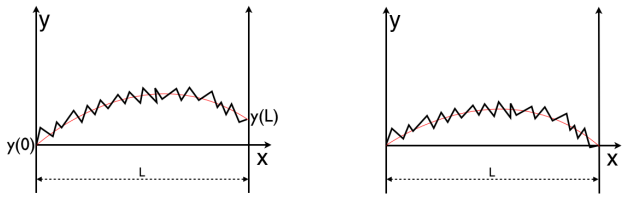

(a) Before levelling. (b) After levelling.

Figure 5.5: Illustration of the computational levelling.

2. Consider the tile had a quadratic profile, which meant the mean line one has used in the code was a quadratic function instead of a straight line. This helped to fix the convexity issue.

The results of this technique will be presented in section 5.4.2.

The parameters used to acquire data on stainless steel tiles can be consulted in table 5.2 and those used for PMMA can be consulted in table 5.3.

Table 5.2: Dektak acquisition parameters for stainless steel tiles.

Stylus Radius /μm	Lenght /μm	Resolution /μm	Force /mg	Duration /s
12.5	500	0.056	1	30

Table 5.3: Dektak acquisition parameters for PMMA layers.

Stylus Radius /μm	Lenght /μm	Resolution /μm	Force /mg	Duration /s
12.5	1000	0.111	1	30

5.3 Reflectance and Transmittance

One shall start by making a small introduction to the spectrophotometry principles involved during this work, with principles available at [55, 56, 57, 58].

Spectrophotometry governs the medium- and matter-effects on the transfer of electromagnetic radiation. The basic processes involved are absorption, reflection and transmission. The current study did not include any absorption measurements, even though it is strictly related with the other two by the relation:

$$\rho + \tau + \alpha = 1 \tag{5.9}$$

as a consequence of the law of conservation of energy and where ρ, τ and α stand for reflectance, transmittance and absorptivity, respectively.

Reflectance can be defined as the relation between incoming (I_0) and reflected (I_R) radiant power, expressed mathematically by:

$$\rho = \frac{I_R}{I_0} \tag{5.10}$$

Similarly, transmittance may be defined mathematically as the relation between incoming and transmitted (I_T) radiant power:

$$\tau = \frac{I_T}{I_0} \tag{5.11}$$

and is directly related to absorptivity by

$$\alpha = log_{10}\left(\frac{1}{\tau}\right) \tag{5.12}$$

Being the principles introduced, one must say that not only had one to smooth the surface of the tiles, but one should also attempt to make it without compromising the stainless steel

identity. In order to evaluate identity loss, reflectance tests have been made on both the raw tiles and the tiles covered with a layer of PMMA. Transmittance tests have also been done on the encapsulating layers with the same purpose.

Reflectance and transmittance tests were done using Shimadzu UV-2100. The main features of this model are those shown in the table below.

Table 5.4: Shimadzu UV-2100 specifications.

Values	Wavelength range/nm	Resolution/nm	Photometric accuracy	Light Source
Possible	190-900	0.1	±0.3%T	Hal.+Deut.
Used	300-800	1	±0.3%T	Hal.+Deut.

Note: "Hal." and "Deut." stand for *Halogen* and *Deuterium*, respectively.

The monochromator of this model is an aberration corrected Zerny-Turner mounting with a high performance blazed holographic grating.

5.4 Results and analysis

As stated before in section 2.1, the Optical Identity Study included roughness, thickness, reflectance and transmittance studies. In this section one will present those results and their analysis in the ambit of this work.

5.4.1 Reflectance of the Stainless Steel Tiles

The first step of this work consisted on analysing stainless steel tiles' reflectance. The company that required this study possesses two types of tiles, polished and unpolished, and wishes to acknowledge which ones suit OLED-usage the best. The tiles' size used was 5x5cm and they were divided in five areas (check scheme below) to understand if reflectance changed significantly over the surface.

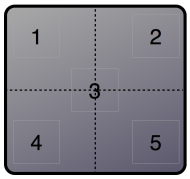

Figure 5.6: Scheme of the tiles' division for reflectance studies.

Using the Shimadzu in the visible range (one wishes to study the loss of steel identity to the human eye) of the electromagnetic spectrum, one acquired data of three polished- and three unpolished-samples, which resulted in chart 5.7. Each line in the chart is the average of the reflectance, for a certain zone, of three tiles belonging to the same group (polished or unpolished).

From the results one can conclude that, as expected, reflectance of the polished samples is higher than those which are not polished. With a quick look one can confirm that while

unpolished tiles possess a reflectance, for all visible wavelengths, in the range of 20%-50%, the polished ones range from 50%-70%.

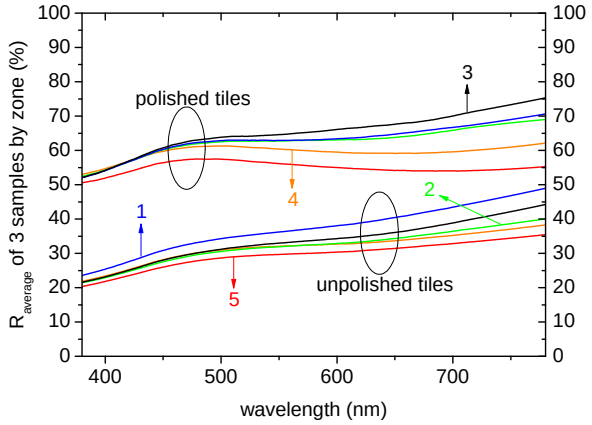

Figure 5.7: Average reflectance in the visible region, by zone, of three polished- and three unpolished-tiles.

A pattern was found, though, in which the middle zone (3) and the top zones (1 and 2) possess the highest reflectance. This may be explained by the marks made by the press-brake the company uses to produce the tiles, which were stronger at the bottom (4 and 5) of the sample. Even though this information alone is already quite informative, it needs to be compared with the chart presenting PMMA's reflectance to be conclusive on whether PMMA significantly changes stainless steel optical identity or not.

5.4.2 Roughness of the Stainless Steel Tiles

Following reflectance analysis, one had to analyse the roughness of the tiles. Only by doing so can one decide the thickness of PMMA to grow on the tile and thus collect data regarding its reflectance. Two polished- and two unpolished-tiles were tested, each group with a 2x2 cm and a 5x5 cm tile; all of them were divided in nine zones to understand if the roughness was constant throughout the whole area of the tile, as shown in figure 5.8.

Figure 5.8: Scheme of the tile's division.

Using the Dektak 150 one acquired results on tiles' morphology in the referred nine zones. But, as explained in section 5.2, the Dektak software does not directly deliver a satisfactory value, hence the referred *MatLab*® treatment. The results of such treatment for the nine studies zones of each tile are presented below from figures 5.9 to 5.12.

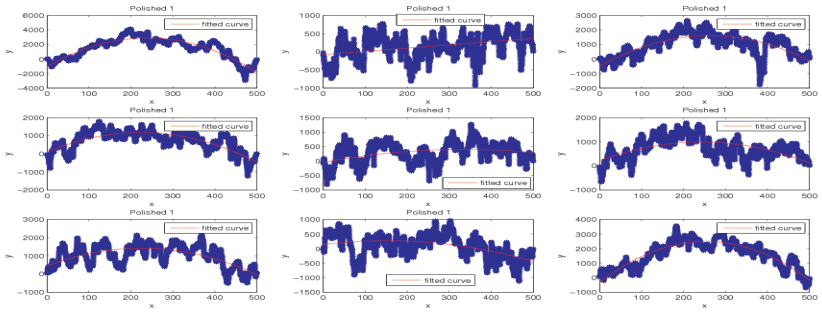

Figure 5.9: Raw data and fitting for the 5x5 cm polished tile (named Polished 1).

In the charts above one can understand how important it was to use a quadratic function as a mean line. It is clear from nearly all individual charts that a straight line would by no mean be a good adjust.

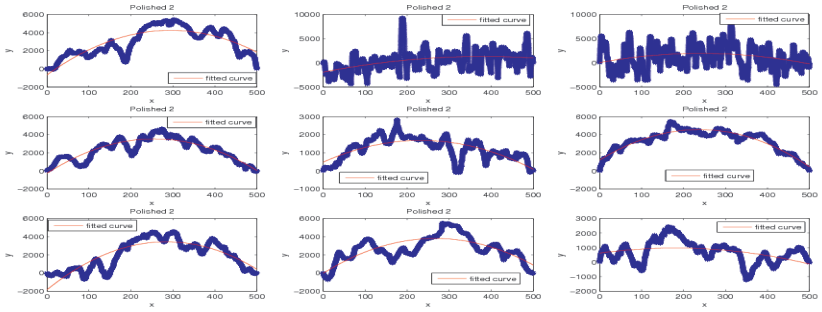

Figure 5.10: Raw data and fitting for the 2x2 cm polished tile (named Polished 2).

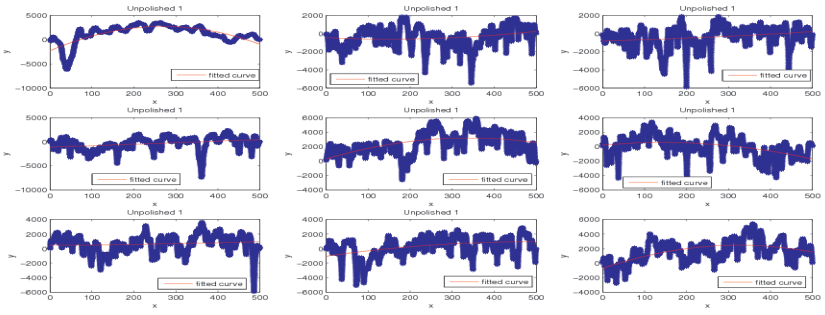

Figure 5.11: Raw data and fitting for the 5x5 cm unpolished tile (named Unpolished 1).

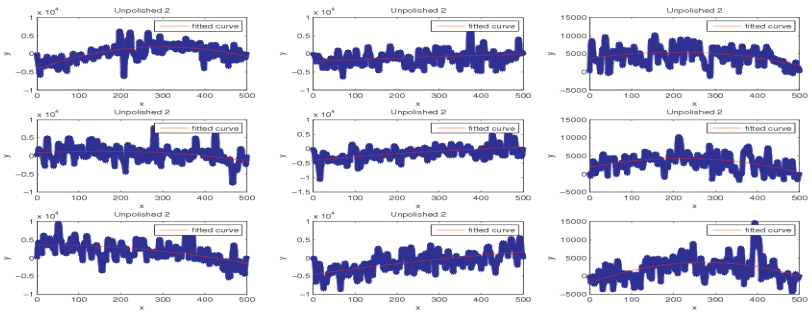

Figure 5.12: Raw data and fitting for the 2x2 cm unpolished tile (named Unpolished 2).

After this analysis the maximum roughness per zone was calculated and is presented in the chart of figure 5.13. It is clear that polished tiles possess a lower roughness than unpolished ones, with exception from the two first points from *Polished 2*, which were attributed to a scratch and not to the polishing process. Thus, taking this and the reflectance data from the previous section in consideration, it was decided that henceforth only polished tiles would be used, since they reflect better and provide less average roughness.

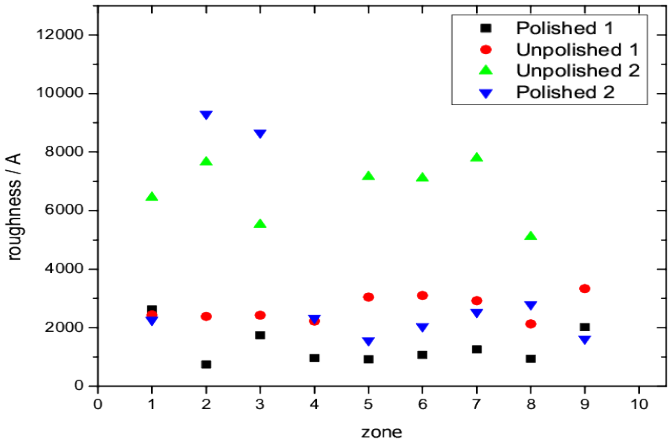

Figure 5.13: Roughness in zones 1-9 of the four tiles analysed.

5.4.3 Thickness of PMMA Thin-films

Based on the results from sections 5.4.1 and 5.4.2, there was now a guideline for the study of PMMA concentration versus thickness. Knowing what PMMA thickness one needs to deposit, a study was performed to identify what concentration had to be used to guarantee a sufficiently thick layer. Therefore, spin-coating depositions of films (with the parameters described in 5.1) with mass/mass concentrations from 1-5% in chloroform solvent have been

done with the outcome which can be consulted in figure 5.14. A linear fit has been added to the chart, with parameters available at table 5.5.

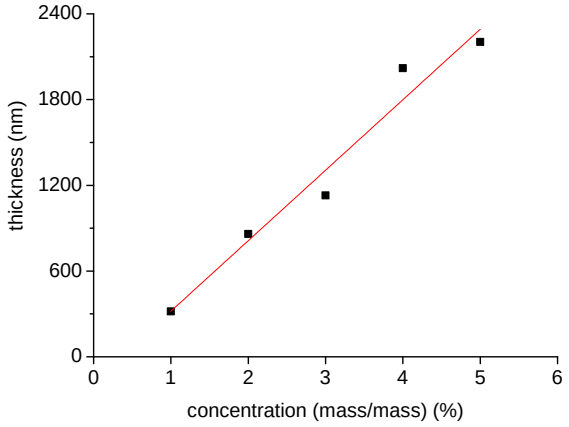

Figure 5.14: Thickness of PMMA as a function of its concentration.

The parameters obtained for the linear fit can be seen in the table below.

Table 5.5: Parameters of the linear fit presented in figure 5.14

Slope	Slope's standard error	Intersection	Intersection standard error	R^2
$49x10^1$ nm	$5x10^1$ nm	$-2x10^2$ nm	$2x10^2$ nm	0.95

Where R^2 stands for the coefficient of determination.

After these results, one was now in conditions, assuming parameters of deposition were kept constant, to choose a PMMA concentration to smooth any stainless steel surface of interest. However this meant just a part of the work was complete, since reflectance tests had still to be done to evaluate the visual impact of these films on the steel.

5.4.4 Reflectance of PMMA Thin-films

Using the same concentrations from 5.4.3, five PMMA thin-films deposited on polished tiles were optically analysed using the Shimadzu. The following data has meaning, in the ambit of this work, only if compared with figure's 5.7 data, since it is this comparison that the company will appreciate.

One must stress that the Shimadzu acquires specular reflectance data and not diffuse reflectance, which would be the appropriate technique to compare with the human eye. An integrating sphere has been used to overcome this, since it collects radiation reflected in any angle. And to enhance the quality of the results, the light source used was a solar simulator, which is the closest to natural illumination. The results are presented in figure 5.15b, where data from stainless steel without any additional layer was used as a reference for convenience of interpretation.

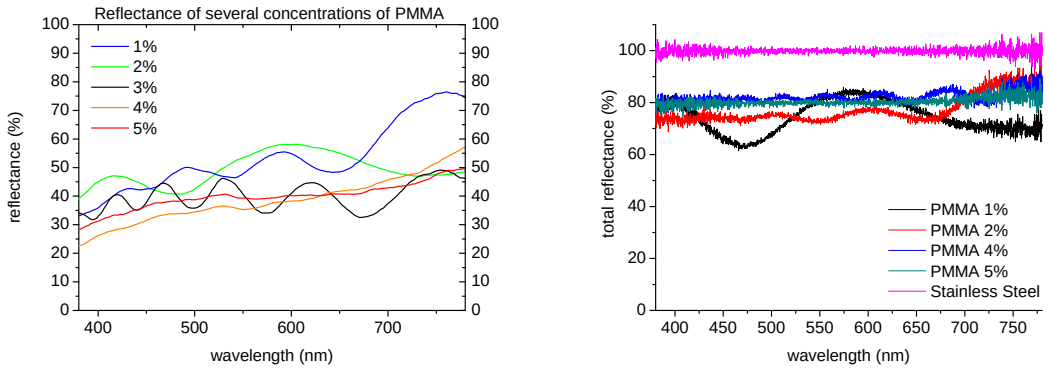

(a) (b)

Figure 5.15: a) Reflectance of PMMA as a function of its concentration. b) Reflectance, measured with an integrating sphere, for several PMMA concentrations deposited over a polished stainless steel tile. Data acquired with a stainless steel tile, without PMMA, as reference.

By looking at 5.15a, interference phenomena is clear for all the concentrations studied, and it is particularly strong for the 1-3% concentration range. The pattern appears because when radiation hits the stainless steel tile, it is reflected back through the PMMA layer. However, when it reaches the PMMA/air interface, some is reflected again against the tile and other is *freed* into the air. As explained in section 5.1.1, this makes the interference pattern visible. In the ambit of this work, this is treated merely as an observation and no more considerations shall be made.

5.5 Conclusions

Looking at the data regarding the roughness of the tiles, presented in section 5.4.2, one found that a safe thickness for a smoothing layer would be less than 1 μm, since no roughness above this quantity was identified. Confronting with the data from section 5.4.3, a PMMA concentration of 3% or higher would then be required to properly cover the tile.

Figure 5.15 offers valuable information regarding the loss of reflectance when PMMA is deposited. By illuminating the tiles covered with PMMA with a solar simulator, and collecting reflectance data with an integrating sphere, one can mimic observer's conditions accurately. It seems an average reduction of around 20-30% reflectance is the minimum optical damage that can be inflicted. To the naked eye, at a distance of an arm or greater, stainless steel tiles and the ones with PMMA are undistinguishable.

Chapter 6

Atmospheric Exposition Study

6.1 Encapsulation Methods

Two distinct encapsulation barriers have been used in this work: ordinary glass as a reference and a *Ceramis*® SiOx barrier film with PET (poly(ethylene terephthalate)), a flexible, ultra-thin layer manufactured by Alcan Packaging [60].

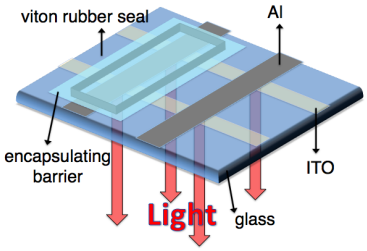

(a) Perspective of an encapsulated OLED.

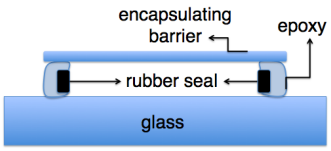

(b) Sectional view of the encapsulation technique.

Figure 6.1: A typical OLED used in this work in perspective and a detailed sectional view of its encapsulation.

A general top view of a common OLED one has used is provided in figure 6.1a. After the OLED was withdrawn from the evaporator, it was kept under a N_2 (nitrogen) flow in order to protect the device from oxygen and water vapour attacks. All the encapsulation processes which shall be described below were done in that environment.

A rectangular rubber frame was used as a way to avoid touching the emissive zone with the barriers, as show in figure 6.1a. Epo-Tek® 302-3M epoxy was used either as glue and lateral barrier, as explained visually in 6.1b. The rubber frame, properly soaked in epoxy and with the desired barrier already applied on it, was then carefully placed in the right position. Following these steps, the epoxy and the OLED were taken to an oven, with uncontrolled environment, to cure the epoxy at 50^{o}C for 3h30m as recommended.

6.1.1 Transmittance of the Encapsulating Barriers

In order to evaluate how each barrier affects the radiation emitted by the OLED, one performed transmittance measurements with the Shimadzu. The results are as follows:

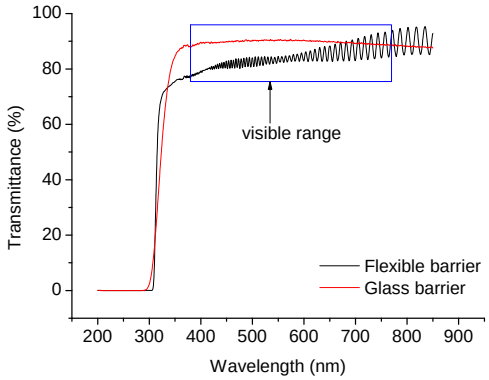

Figure 6.2: Transmittance of glass and flexible barrier.

The first immediate observation has to due with an interference pattern in the results regarding the flexible barrier, resultant from the several PET/SiO_x layers used in its construction. Since PET is very transparent in SiO_x is partially reflective, the effect arises.

One concludes from figure 6.2 that between 380-650 nm, a significant part of the visible range, glass is more transparent than the flexible barrier. This can (and will) have repercussions in upcoming interpretations, and shall be recalled in the appropriate moment (section 6.3.1).

6.2 Construction of the Measurement System

The experimental apparatus represented in fig. 6.4 was developed in order to allow one to acquire the desired spectra spectra quasi-simultaneously on both emitting OLEDs using Ocean Optics, as well as current measurements.

As such, an optical fibre, with a collimating lens which captured all the emissive area, needed to be shifted from one OLED to the other, spectra had to be acquired when the alignment was perfect and current intensity had to be measured in that moment. To accomplish such task, a measurement system was designed and included:

1. Function Generator from TTi, Model TG2000;
2. Digital Delay / Pulse Generator from Stanford Research Systems, Model DG535;
3. Electric board with a quad 2-input NAND gate, Model HEF4011B, and respective electric circuit.
4. Keithley SourceMeter, Model 2425;
5. Keithley SourceMeter, Model 2611;

6. Spectrometer from Ocean Optics, Model USB4000;
7. Osciloscope from UNI-Trend, Model UT2102C;
8. Disc tray adapted to switch the optical fibre (from the Ocean Optics system) between the two OLEDs (encapsulated and not encapsulated).

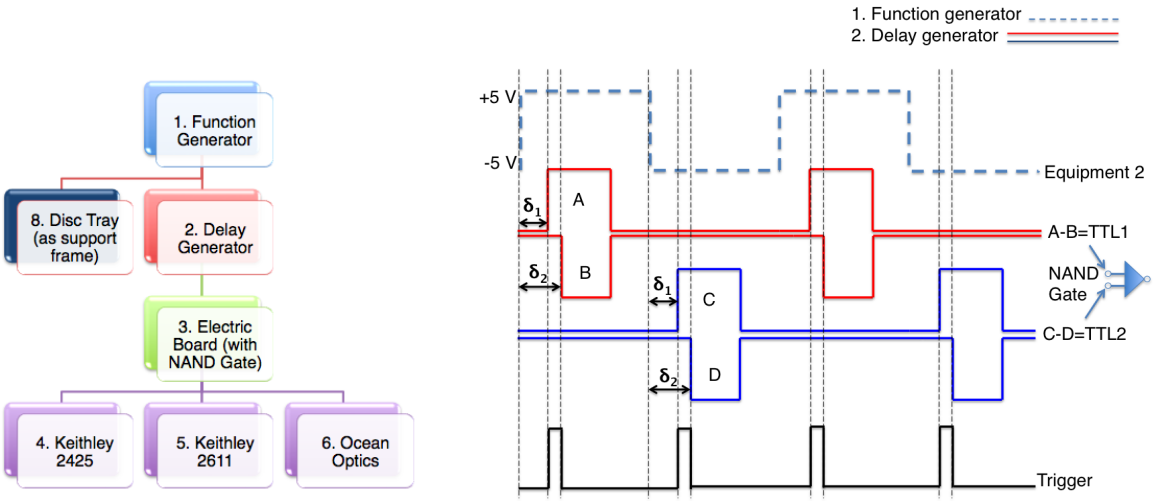

(a) Equipment connections.

(b) Time diagram.

Figure 6.3: a) Diagram representing the equipment connections. b) Diagram representing the trigger line creation process.

Using diagram 6.3a one can explain the connections: the square wave generated by *1* is sent either to *2* and to control *8*'s movement (the fibre is coupled to the place where the laser of the Disc Tray used to be - it moves left or right when the signal is positive or negative). Equipment *2* uses that signal to generate a TTL pulse both for positive (TTL1) and negative (TTL2) parts of the square waves of *1*, sending those TTL pulses to the HEF4011B (NAND Gate) where they are combined (TTL1+TTL2). Therefore the HEF4011B output (the trigger line) is then able to control the acquisition of *4*, *5* and *6*, synchronized with the movement of the optical fibre.

The diagram 6.3b is a visual demonstration of the processes needed to achieve the desired trigger line (in black) using the delay generator. The equipment offers the possibility for one to generate four different lines (A to D) and to make basic arithmetic operations between them.

Signal A was chosen to start a delay δ_1 after the rise of the square wave which came from the function generator and to end before its fall. On the other hand, signal B started with a delay relatively to signal A, given by $\delta_2 - \delta_1$, but ended at the exact same time. This meant one could subtract them and obtain *TTL1*. Signals C and D worked in the exact same way, but for the negative part of the original square wave, allowing one to obtain *TTL2*. By combining *TTL1* and *TTL2* with the NAND Gate, one obtained the trigger line necessary to control equipments *4*, *5* and *6*.

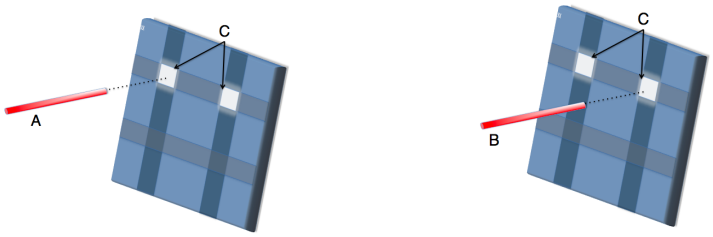

(a) Fibre in position A. (b) Fibre in position B.

Figure 6.4: Fibre's movement scheme between two emitting OLEDs.

6.2.1 Electrical Measurements

For current intensity measurements one used Keithley's SourceMeters 2425 and 2611A. These devices are able to simultaneously provide a chosen voltage and measure the flowing current down to the pA-scale if needed, thus being indicated for the desired measurements [61, 62]. Since all the OLEDs have the same structure and dimensions, the current intensity and the current density are proportional, i.e., $i(t) \propto J(t)$.

Acquisition was controlled by the external signal (trigger) generated by the NAND gate.

6.2.2 Optical Measurements

Optical data was acquired using Ocean Optics USB4000 Spectrometer with the following parameters:

Table 6.1: Ocean Optics acquisition parameters.

Spectral Range	Number of pixels	Spectral Resolution	Integration Time
200-890 nm	3648	1.2 nm	200 ms

In some experiments, due to technical issues related to the reception of the trigger signal by the Ocean Optics hardware, one had to acquire spectra manually. This does not invalidate in any manner the data acquired, the only consequence is a lower frequency of experimental points. The remaining work went as described.

6.3 Results and Analysis

This section is divided in three major subsections: *OLED's Characterization*, *Emission Degradation: Raw Data*, which presents data without any treatment or manipulation, and finally *Emission Degradation: Analysis*, which consists mostly of treated data, indirect measurements and their analysis.

6.3.1 OLED's Characterization

IV and luminance curves.

Using a Keithley SourceMeter one can easily obtain intensity vs voltage (IV) data, which is an essential initial study for OLED's characterization (for example, to determine the tension at which electric current starts to flow significantly).

On the other hand, it is of extreme interest to correlate such chart with one such as luminance vs voltage - LV, thus allowing one to completely connect the dependency of luminance with electric current. For that, one recorded a movie from the OLED under operation (during the IV test) using a microscope with a coupled camera. The camera captured a total area A_T bigger than the emitting area, A_E. For each movie frame there are N pixels, each one located at a coordinate (x,y). Every pixel has three colour components from the RGB (Red-Green-Blue) colour model, which emit individually and the camera records it. By adding the there components $\Psi_R + \Psi_G + \Psi_B$ for a certain position (x,y), one obtains a quantity proportional to the brightness of the corresponding pixel, which is also proportional to its luminance. By repeating the process for every single pixels, one can calculate the total luminance in arbitrary units. And by repeating it for a desired number of frames, one can calculate the luminance over time. The fact that $A_T > A_E$ does not constitute a problem, since the colour coordinates are zero for the non emitting area. However, it was necessary to guarantee that the camera's CCD was not saturated during the acquisition, so the exposition parameters have been adjusted accordingly and have not been changed during all the measurements performed.

Luminance in arbitrary units, as explained in the previous paragraph, was calculated from the following relation:

$$L \propto \sum_{\beta=R,G,B} \sum_{x,y} \Psi_\beta(x,y) \tag{6.1}$$

The results can be found below.

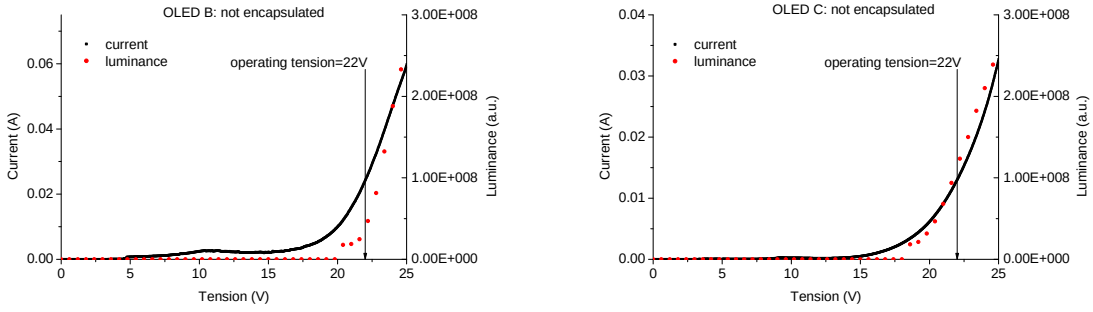

(a) OLED B.

(b) OLED C.

Figure 6.5: I=f(V) and L=f(V) chart for not encapsulated OLEDs.

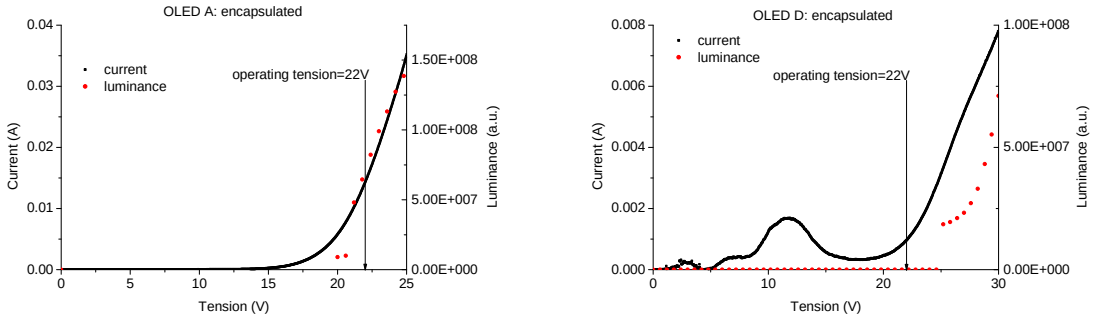

(a) OLED A.

(b) OLED D.

Figure 6.6: I=f(V) and L=f(V) chart for encapsulated OLEDs (flexible barrier).

Regarding the previous four charts, IV and LV behave as expected. That means one expected a strong correlation, even proportionality, between the current intensity flowing through the OLED and its luminance. It is clear, though, that many differences become evident when looking at such charts, both in current behaviour and luminance behaviour. While luminance data might be affected by the determination method (specially at low levels of brightness), current intensity is certainly not exposed to that kind of uncertainty. Even if one disregards luminance measurements for one moment, and focus on current only, strange behaviours are particularly visible in figures 6.5a and 6.6b. Figure 6.6b is completely atypical, since its current starts rising before 5V and it only starts emitting at around 25V. One has attributed that behaviour to a misconception of the device. One can infer from IV and LV curves that the reproducibility of devices' properties is very low, and that shall be taken into account in future considerations.

Henceforth, all the tests will be done under an operation tension of 22V, since it represents the zone where $I \propto V$ and no saturation occurs.

Electro-luminescence for t=t$_0$

One has also acquired spectral data with the system described in 6.2. By gathering spectra on a frequent basis one can latter determine the luminescence decrease over time and the spectral deviation, if it exists. For now, one shall present the spectra for t=0 s for both encapsulated and not encapsulated OLEDs.

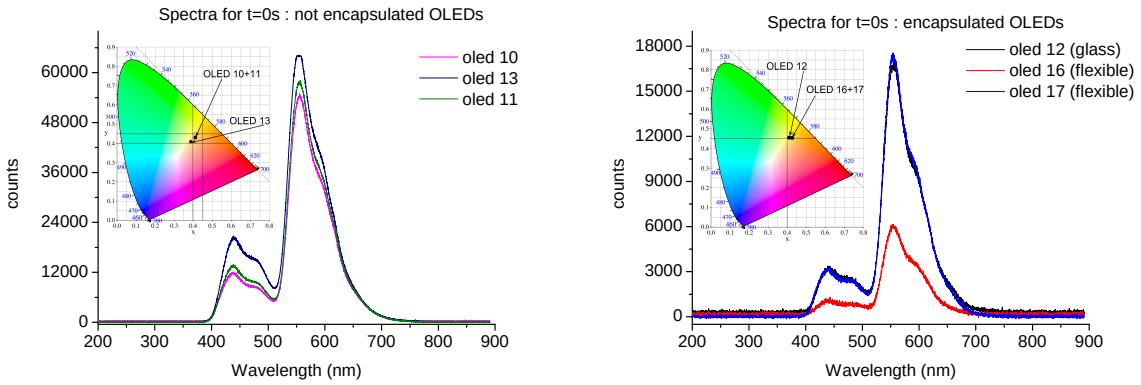

(a) Not encapsulated OLEDs.

(b) Encapsulated OLEDs.

Figure 6.7: Spectra for t=0s for (a) not encapsulated and (b) encapsulated OLEDs.

Two main peaks of emission are observed, at around 440 nm and 560 nm. According to Huang et al [63], who have built and studied an OLED with the very same organic layers, those peaks are from NPB (blue emission) and Rubrene (yellow emission), respectively. Photoluminescence tests with the exact same results proved that such emisisions belonged to the species. According to the same work, the expected 525 nm emission from Alq_3 is not seen as a consequence of BCP's hole-blocking properties.

From the CIE colour coordinates (CIE 1931 standard) figures attached to the charts, one can conclude there are small colour changes on the observed emission from the OLEDs. As already stated previously, the reproducibility of these devices is hard to maintain, and that should be one of the reasons behind the CIE-coordinates spread. Plus, from figure 6.2, one knows the barriers, mainly the flexible one, absorb blue radiation. Considering the optical sensor is obviously *out* of the OLED, i.e., after the barrier, one cannot directly determine what the organic layers are really emitting. Consequently, a red-shift occurs as a result from the lack of blue-transparency from the flexible barriers.

6.3.2 Emission Degradation: Raw Data

Spectra over time

As described in 6.3.1, one has acquired spectral information frequently to allow a full optical characterization in what concerns to degradation. One will now present data, OLED-by-OLED, for three given times which represent 1) the initial emission, 2) an emission where the peak is between 25-50% of the initial value and 3) an emission in which the number of counts is so low one can hardly identify the higher energy peak. In the next section, all the spectra (for all the instants available) will be treated and discussed.

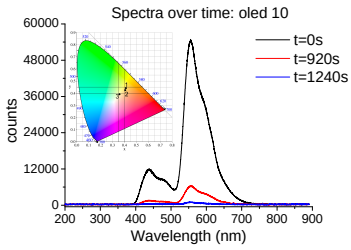

(a) OLED 10: not encapsulated.

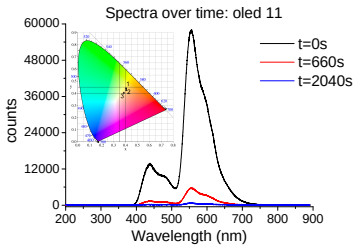

(b) OLED 11: not encapsulated.

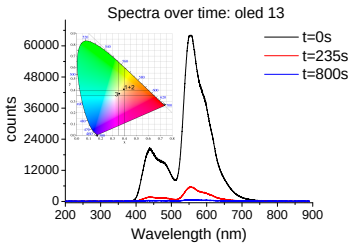

(c) OLED 13: not encapsulated.

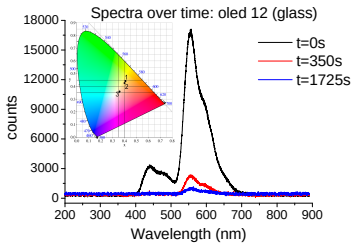

(d) OLED 12: encapsulated with glass.

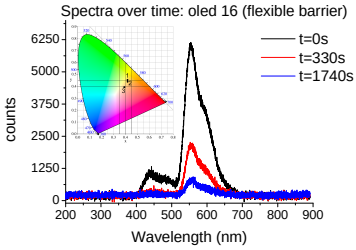

(e) OLED 16: encapsulated with flexible barrier.

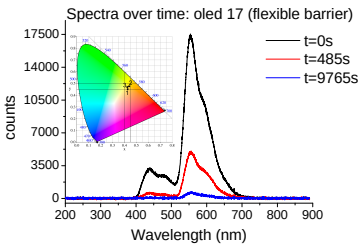

(f) OLED 17: encapsulated with flexible barrier.

Figure 6.8: Spectral shape over time.

The conclusion withdrawn from the previous charts is that the electronic states involved in the recombination process do not change over time. If it happened the peaks would have a wavelength-shift. Also, a detailed analysis of spectral shape over time (not shown here) has confirmed that no other spectral bands appears, in particular the one at 525nm from an eventual Alq_3 emission. However, it is clear from the CIE diagrams that the CIE-coordinates move over time. Since the emission results from a combined NPB and Rubrene emission, one can only deduce that the degradation rate of both emissive species is different, thus affecting the colour as the OLED degrades.

Current over time. Luminance over time.

Using the system described in 6.2 one was able to collect data regarding OLED's electrical current over time, I(t). Furthermore, by integrating the spectra shown in 6.3.2, for all given times, one can calculate the luminance over time, L(t), in arbitrary units. Even though this cannot be technically called *raw data*, since it involves computational processing, one opted for showing it in this section to allow a direct comparison with the current intensity chart. For both encapsulated and not encapsulated groups, the correspondent charts are presented.

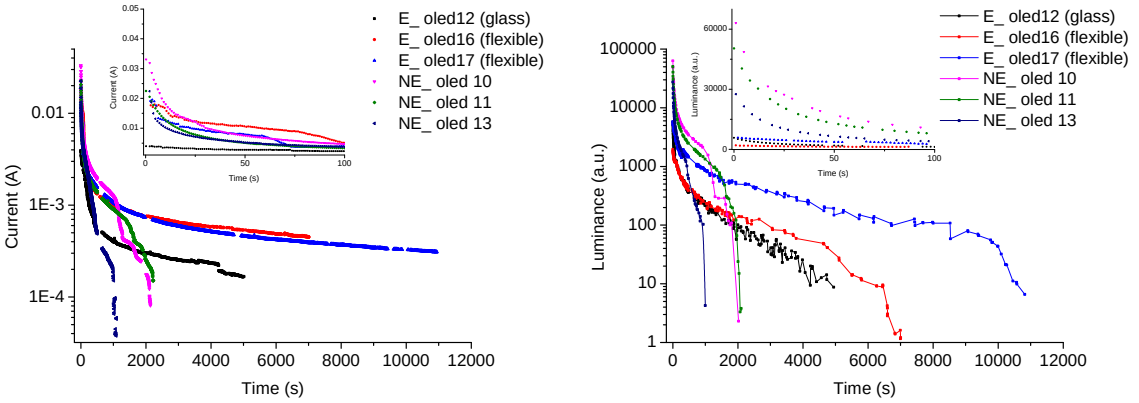

(a) Current over time.

(b) Luminance over time.

Figure 6.9: (a)I(t) and (b)L(t) charts for encapsulated (E) and not encapsulated (NE) OLEDs. Barrier type is between brackets.

Initial electric current and luminance differ greatly from device to device. Once again, the lack of construction reproducibility is attributed as the reason for this. However, considerations regarding the two previous charts will be made in the next section, where their analysis will take place.

6.3.3 Emission Degradation: Analysis

Dark-spots

After performing the IV and LV tests presented in section 6.3.1, one used the same camera to analyse encapsulated and not encapsulated OLEDs as they degraded. This should allow a study on dark-spot appearance. The results are represented in the figures below:

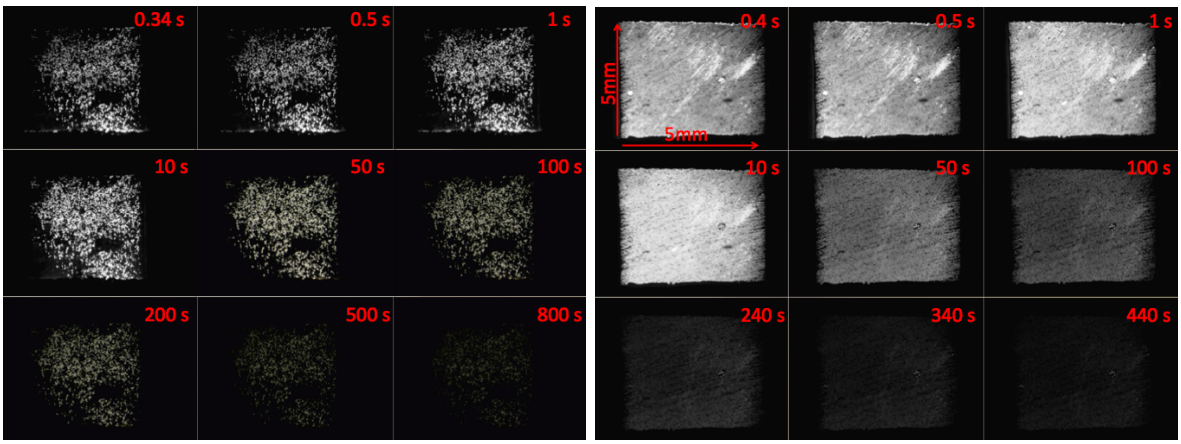

(a) Encapsulated OLED. (b) Not encapsulated OLED.

Figure 6.10: Dark-spots analysis over time for (a)encapsulated and (b)not encapsulated OLEDs.

Unlike expected, there does not seem to exist an increase in dark-spots number as the OLED degrades; instead, they appear to exist from the very beginning of operation time. What one observes is a simple loss of brightness, which is proportional to luminance. Even though the encapsulated OLED starts with an unusual number of dark-spots, it lasts nearly twice the time. One must emphasize that the OLEDs lifetime was not what is visible in the previous figure; since the acquisition parameters had to be adjusted to allow the camera's CCD to avoid saturation, the emission stops being detected by the camera's sensor while it is still visible for an observer. Still, the aim of this study was to observe an eventual appearance of dark-spots, which did not happen.

The fact that so many dark-spots are already present when the OLED is turned on leads one to conclude that there are several defects during its growth. Furthermore, the lack of appearance of new dark-spots during the study performed suggests that the usual processes responsible for them - such as molecular migrations, delamination or *bubbles* in the electrodes - are not observed.

Normalized current over time. Normalized luminance over time. Part 1.

Since the initial electric current consumed by the OLEDs seems rather random, and the interest of this work is to determine how it evolves over time and not how high/low it is at the beginning of operation, one has decided to analyse electric current data normalized. The same principle was used to study the luminance data.

Given the nature of the processes involved, the y-axis has been converted to logarithmic, this way enhancing certain behaviours.

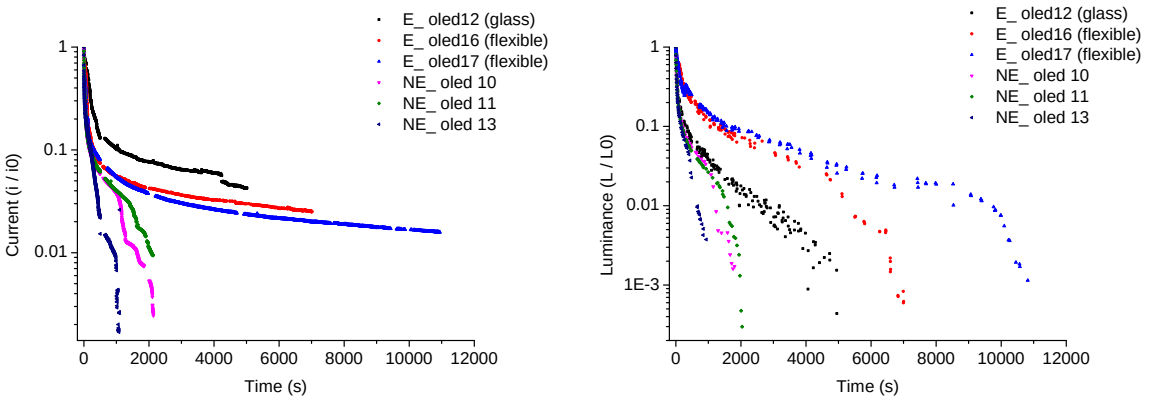

(a) Normalized current over time.

(b) Normalized luminance time.

Figure 6.11: (a)Normalized current and (b)normalized luminance over time for encapsulated and not encapsulated OLEDs.

There seems to be a clear pattern that distinguishes the encapsulated OLEDs from the not encapsulated, and also a particular pattern between the two OLEDs encapsulated with the flexible barrier. The differences between devices of the same group were attributed to the variability in their construction.

Henceforth, for ease of interpretation, only one OLED of each group will be analysed: OLED 11 will represent the not encapsulated group, OLED 12 will represent OLEDs encapsulated with glass and OLED 16 will represent the ones encapsulated with the flexible barrier.

Luminance as a function of electric current

Before moving onto a deeper analysis of the previous latest results, one shall introduce a chart where luminance is presented as a function of electric current for the three OLEDs.

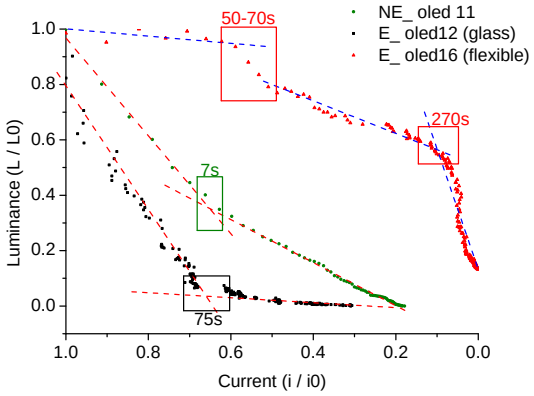

Figure 6.12: Normalized luminance as a function of electric current.

The x-axis has been adjusted for convenience; as the experimental points *move* to the right, the current decreases but the time of operation increases. Plus, dashed lines were added as visual helpers.

It is clear that the luminance of the OLED encapsulated with the flexible barrier is much less dependent from the current than the others, particularly when luminance is still >50%, which is extremely important since this percentage is the industry standard to define OLEDs' lifetime. It presents three clear distinct regimes, in which the first one shows a small dependence of the luminance with the current. The device encapsulated with glass, on the other hand, only presents two regimes - one of high luminance/current dependency and one where the luminance depends from the current much less. The OLED not encapsulated also presents two distinct regimes, but both appear to represent a high dependence from the luminance with the current flowing.

Interest times have been chosen to identify regions where a change in behaviour is likely to be happening, and that shall be further analysed in the next section.

Normalized current over time. Normalized luminance over time. Part 2.

For the construction of figures 6.13a and 6.13b, charts from figure 6.11 were adjusted so time would range from 0-200 s; additionally, the interest points from figure 6.12 were added. From figures 6.11 and 6.13, it seems evident that one degradation process is common

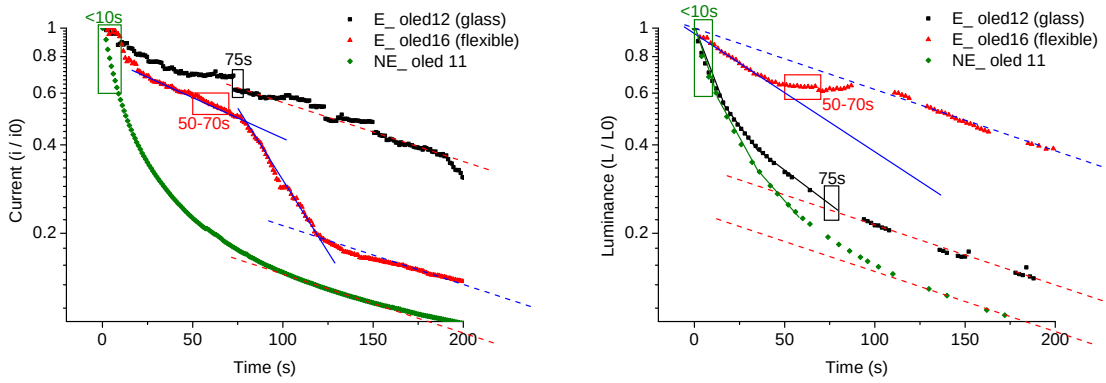

(a) Normalized current over time.

(b) Normalized luminance over time.

Figure 6.13: Initial 200 s of (a) normalized current and (b) normalized luminance over time.

to all the OLEDs. Dashed lines have been added to figs. 6.13a and 6.13b to highlight regions where the trend lines have the exact same slope. This process is clearly responsible for the late degradation of the current and the luminance. Other processes, which seem to be dependent from the encapsulation, completely dominate the fast degradation of the OLED in the initial 100-150 s. As a direct consequence, both barriers seem to essentially act upon these initial processes, delaying them or decreasing their intensity. From time times withdrawn from figure 6.11 and marked in figure 6.13, one can identify behaviour changes for the encapsulated OLEDs, as expected. For the one not encapsulated it is not clear, probably because several processes might be happening in such a short period of time. But on the others, however, one can doubtlessly affirm there is a change, both for charts 6.13a and 6.13b.

These behaviour shifts can be interpreted as times where the governing degradation process changes, disappears or a new one appears.

One knows from the literature that a high quality OLED has a working temperature of $\sim 60^o$C and that the glass transition temperature of NPB is $T_g \approx 95^o$C. However, morphology changes occur sooner, at around 45 ^{o}C, as long as the temperature is kept that high during a long time or even as fast as 5 minutes - in the presence of moisture [26, 64, 65]. Provided with this information, it seems reasonable to state that morphological changes in NPB conducing to crystallization are the common process for all the OLEDs' late degradation. This should not apply for Alq_3 considering its T_g of approximately $\sim$130-140 ^{o}C. Therefore, the dashed lines in the figures above are a representation of this common process, which begins to govern the three OLEDs after roughly 100 s. The flexible barrier appears to be the most effective in delaying this phenomenon.

It is evident that even though the current decreases slower in the OLED encapsulated with glass, that does not translate into a better luminance, which is in line with the conclusions from the analysis of figure 6.12. However, why such differences of dependency happen is what will be discussed next.

Different thermal conductivities characterize the encapsulating barriers: while soda-lime glass has a $\kappa = 1\ Wm^{-1}K^{-1}$, PET has a $\kappa = 0.28\ Wm^{-1}K^{-1}$ and SiO_2 has a $\kappa = 1.4\ Wm^{-1}K^{-1}$ [66, 67, 68]. Considering the barrier is mostly constituted by PET, it should have a lower thermal conductivity than the glass (it is not provided by the manufacturer). However, the glass used has around 2 mm in thickness, while the flexible barrier should have no more than a few dozen μm. For the remaining interpretation, one assumes that the glass barrier is not capable of dissipating as much heat as the flexible barrier.

The overall electro-luminescence flux, temperature dependent, is given by:

$$\Phi_{EL}(T) = \alpha \eta_{PL}(T) P(d) \mu_p F(d) \tag{6.2}$$

where α is a constant, η_{PL} is the photo-luminescence efficiency, μ_p is the hole mobility, F(d) is the electric field at a distance d and P(d) is the hole density at the organic heterointerface [69].

On one hand, assuming glass is a poor thermal dissipater in the referred conditions, the OLED it is protecting will warm up faster. According to 3.4, this will increase the carrier mobility in the organic layers. Consequently, the electric current will remain higher due to this process.

On the other hand, the photo-luminescent efficiency can be decreased by two main factors: probability of recombination and appearance of trapping-centres. With the temperature rising, the probability of recombination decreases because non-radiative processes are favoured. Additionally, trapping-centres prevent electrons from even reaching the recombination zone [69, 70].

This is the most likely explanation for the fact that the OLED encapsulated with glass possesses a slower current decrease but a higher luminance decrease, rendering the flexible barrier more effective.

Chapter 7

Conclusions and Future Work

General Conclusions of the Optical Identity Study

One has found that, in order to guarantee that the stainless steel tiles are completely smoothed and insulated, a PMMA layer of $\sim 1\mu$m is needed, which corresponds to a PMMA concentration of at least 3% according to the used spin-coating parameters.

PMMA on stainless steel reduces the reflectance between 20-30%, depending on the wavelength and concentration desired, which could compromise steel's identity. However, one confirmed that at a relatively short distance of ∼50-60 cm, steel tiles with and without PMMA are virtually undistinguishable to the naked eye.

From one's point of view, PMMA is an effective smoothing and insulating barrier to be used as the first layer of an OLED on top of stainless steel, considering the low loss of optical identity requirement.

General Conclusions of the Atmospheric Exposition Study

The flexible barrier studied proved effective, allowing a substantial rise in the OLED lifetime (luminance >50% of the initial) of roughly one order of magnitude. Even though the glass barrier has clearly delayed the degradation, the flexible one has overcome it.

By looking at the luminance data (which is the more important indicator considering this a lighting device), it is evident that the flexible barrier is more capable of delaying certain degradation processes, allowing the luminance to fade at a much slower rate. In the OLEDs studied, the highest luminance in absolute numbers (not normalized) also belonged to the devices protected by this flexible barrier, suggesting it blocked the pre-operation degradation more effective as well.

Even though there is a slight colour change as a consequence of the transmittance properties of the flexible barrier, one considers it a viable choice to be used as the final layer of an OLED built on stainless steel for decoration purposes.

Future Work Suggestions

Growing and encapsulating OLEDs in a controlled environment (e.g. N_2) is an absolute need for future works. This would allow a control of several parameters such as H_2O or O_2 concentrations, which one was not able to control. By ruling them out, any conclusions would be easier and more accurate to make.

Also, the encapsulating process itself would have to be automatized, to avoid excessive

epoxy amounts. The effects of the epoxy on the organic layers could also be part of a future work.

Another suggestion is, assuming the controlled environment referred, to monitor the OLEDs' temperature over time and study the exact correlation. Controlling the temperature and study the repercussions on the OLED would also be interesting.

Bibliography

[1] A. Bergh, G. Craford, A. Duggal, and R. Haitz. The promise and challenge of solid-state lighting. *Physics Today*, 54:42–47, 2001.

[2] S.M. Sze and Kwok K. Ng. *Physics of Semiconductor Devices*. John Wiley & Sons, 2007.

[3] Displaysearch oled display forecast. `http://www.oled-info.com/displaysearch-oled-display-forecast-table`, October 2011.

[4] NanoMarkets. Positioning oled lighting for success. (Whitepaper), 2009.

[5] V.M. Silva and L. Pereira. The nature of the electrical conduction and light emitting efficiency in organic semiconductors layers: The case of m-mtdata - npb - alq3 oled. *Journal of Non-Crystalline Solids*, 352:5429–5436, 2006.

[6] J.H. Lee, J.J. Huang, C.C. Liao, P.J. Hu, and Y. Chang. Operation lifetimes of organic light-emitting devices with different layer structures. *Chemical Physics Letters*, 402:335–339, 2005.

[7] S.D. Theiss and S. Wagner. Amorphous silicon thin-film transistor on steel foil substrates. *IEEE Electron Device Letters*, 17(12):578–580, 1996.

[8] C. Wu, S. Theiss, G. Gu, M. Lu, J. Sturm, S. Wagner, and S. Forrest. Integration of organic led's and amorphous si tft's onto flexible and lightweight metal foil substrates. *IEEE Electron Device Letters*, 18(12), 1997.

[9] J. Cheon, J. Choi, J. Hur, J. Jang, H. Shin, J. Jeon, Y. Mo, and H. Chung. Active-matrix oled on bendable metal foil. *IEEE Transactions on Electron Devices*, 53(5), 2006.

[10] Juhn-Suk Yoo et al. Highly flexible am-oled display with integrated gate driver using amorphous silicon tft on ultrathin metal foil. *Journal of Display Technology*, 6(11), 2010.

[11] Ta-Ko Chuang et al. Top-emitting 230dots/in. active-matrix polymer light-emitting diode displays on flexible metal foil substrates. *Applied Physics Letters*, 90, 2007.

[12] K.R. Sarma, J. Roush, J. Schmidt, C. Chanley, and S. Dodd. Flexible active matrix organic light emitting diode (am oled) displays. In *Asian Symposium on Information Display (ASID)*, 2006.

[13] S. Chung, J.H. Lee, J. Jeong, J.J. Kim, and Y. Hong. Substrate thermal conductivity effect on heat dissipation and lifetime improvement of organic light-emitting diodes. *Applied Physics Letters*, 94, 2009.

[14] Wolfgang Brütting. *Physics of Organic Semiconductors*. Wiley-VCH, 2005.

[15] A. J. Heeger. *Semiconducting and Metallic Polymers: The fourth generation of polymeric materials*, volume 105. Journal of Physical Chemistry B, 2001.

[16] H. Yersin, R. Beaulac, and K.L. Bray. *Transition Metal and Rare Earth Compounds*, volume III. Springer, 2004.

[17] A. Bakulin, D. Martyanov, D. Paraschuk, P. van Loosdrecht, and M. Pshenichnikov. Charge-transfer complexes of conjugated polymers as intermediates in charge photogeneration for organic photovoltaics. *Chemical Physics Letters*, 482:99–104, 2009.

[18] H. Bassler. Charge transport in disordered organic photoconductors: a monte carlo simulation study. *Physica Status Solidi*, 175:15–56, 1993.

[19] L. Kaake, P. Barbara, and X.Y. Zhu. Intrinsic charge trapping in organic and polymeric semiconductors: A physical chemistry perspective. *The Journal of Physical Chemistry Letters*, 1:628–635, 2010.

[20] Z.R. Li and H. Meng. *Organic Light-emitting Materials and Devices*. Taylor & Francis, 2006.

[21] M. Csele. *Fundamentals of Light Sources and Lasers*. John Wiley & Sons, 2004.

[22] Organic/organic heterojunctions in oleds, university of washington. `http://depts.washington.edu/cmditr/modules/oled/organicorganic_heterojunctions_in_oleds.html`, December 2011.

[23] G. Wiederrecht. *Handbook of Nanoscale Optics and Electronics*. Elsevier B.V., 2010.

[24] J. Shinar and V. Savvateev. *Organic Light-emitting devices: a Survey*. Springer, 2003.

[25] H. Ishiia nd K. Sugiyama, E. Ito, and K. Seki. Energy level alignment and interfacial electronic structures at organic/metal and organic/organic interfaces. *Advanced Materials*, 11(8):605–625, 1999.

[26] Junji Kido. High performance oled materials and devices for general lighting. In *VII International Krutyn Summer School*, 2010.

[27] A. Badano, M. Flynn, and J. Kanicki. *High-Fidelity Medical Imaging Displays*. SPIE, 2004.

[28] J.H. Lee, D. Liu, and S.T. Wu. *Introduction to Flat Panel Displays*. Wiley, 2008.

[29] Z.D. Popovic and H. Aziz. Reliability and degradation of small molecule-based organic light-emitting devices (oleds). *IEEE JOURNAL ON SELECTED TOPICS IN QUANTUM ELECTRONICS*, 8(2):362–371, 2002.

[30] F. So and Denis Kondalov. Degradation mechanisms in small-molecule and polymer organic light-emitting diodes. *Advanced Materials*, 22:3762–3777, 2010.

[31] S.Z. Zardareh and F. Boroumand. Degradation in organic light emitting diodes. *World Academy of Science, Engineering and Technology*, 50:274–277, 2009.

[32] Chi-Ping Liu et al. Molecular migration behaviors in organic light-emitting diodes with different host structures. *Organic Electronics*, 12:376–382, 2011.

[33] D. Zou, M. Yahiro, and T. Tsutsui. Study on the degradation mechanism of organic light-emitting diodes (oleds). *Synthetic Metals*, 91(1-3):191–193, 1997.

[34] T. Yamada, D. Zou, H. Jeong, Y. Akaki, and T. Tsutsui. Recoverable degradation and internal field forming process accompanied by the orientation of dipoles in organic light emitting diodes. *Synthetic Metals*, 111-112:237–240, 2000.

[35] H. Jeong, D. Zou, T. Tsutsui, and C.-S. Ha. Short-term degradation behaviors of light emitting diodes made of polyurethane derivative with large permanent dipoles on the side chain. *Thin Solid Films*, 363:279–281, 2000.

[36] P. Schouwink, A.H. Schäfer, C. Seidel, and H. Fuchs. The influence of molecular aggregation on the device properties of organic light emitting diodes. *Thin Solid Films*, 372:163–168, 2000.

[37] F. Charra, V. Agranovich, and F. Kajzar. *Organic Nanophotonics*. NATO Science Series, 2002.

[38] D. Kosolov, D. English, V. Bulovic, P. Barbara, S. Forrest, and M. Thompson. Direct observation of structural changes in organic light emitting devices during degradation. *Journal of Applied Physics*, 90(7):3242–3247, 2001.

[39] M.S. Xu, J.B. Xu, H.Z. Chen, and M. Wang. Nanoscale investigation of moisture-induced degradation mechanisms of tris(8-hydroxyquinoline) aluminium-based organic light-emitting diodes. *Journal of Applied Physics D: Applied Physics*, 37:2618–2622, 2004.

[40] Y. Shen, A. Hosseini, M. Wong, and G. Malliaras. How to make ohmic contacts to organic semiconductors. *Chemical Physics and Physical Chemistry*, 5:16–25, 2004.

[41] A. Muckl, S. Berleb, W. Brutting, and M. Schwoerer. Transient electroluminescence measurements on organic heterolayer light emitting diodes. *Synthetic Metals*, (111-112):91–94, 2000.

[42] L.F. Santos et al. Observation of persistent photoconductivity in vanadyl phthalocyanine. *Journal of Applied Physics D: Applied Physics*, 41, 2008.

[43] J. Laubender, L. Chkoda, M. Sokolowski, and E. Umbach. The influence of oxygen and air on the characteristics of organic light-emitting devices studied by in vacuo measurements. *Synthetic Metals*, (111-112):373–376, 2000.

[44] H. H. Fong and S. K. So. Effects of nitrogen, oxygen, and moisture on the electron transport in tri(8-hydroxyquinoline) aluminum. *Journal of Applied Physics*, 98, 2005.

[45] T.Y. Chu, Y.-H. Lee, and O.-K. Song. Effects of interfacial stability between electron transporting layer and cathode on the degradation process of organic light-emitting diodes. *Applied Physics Letters*, 91, 2007.

[46] K. Wasa, M. Kitabatake, and H. Adachi. *Thin Film Materials Technology: Sputtering of Coumpound Materials*. William Andrew, 2004.

[47] L. Marton and C. Marton. *Methods of Experimental Physics*. Academic Press, Inc, 1979.

[48] M. Petty. *Molecular electronics: from principles to practice*. Wiley, 2007.

[49] Wang Hong, Yu Jun-Sheng, Li Lu, Tang Xiao-Qing, and Jiang Ya-dong. Effect of bcp ultrathin layer on the performance of organic light-emitting devices. *Optoelectronics Letters*, 4(5):317–320, 2008.

[50] S. Baumer. *Handbook of Plastic Optics*. Wiley-VCH, 2010.

[51] G.S. Raghuvanshi. *Engineering Physics*. PHI, 2nd edition, 2010.

[52] Stainless steel: Tables of technical properties. `http://www.euro-inox.org/pdf/map/Tables_TechnicalProperties_EN.pdf`, December 2011.

[53] Material properties of pmma. `http://www.matbase.com/material/polymers/commodity/pmma-cast/properties`, December 2011.

[54] Veeco Instruments. *DEKTAK 150 Surface Profiler User's Manual*, revision a edition.

[55] J.Sole, L.Bausa, and D.Jaque. *An Introduction to the Optical Spectroscopy of Inorganic Solids*. John Wiley & Sons, 2005.

[56] Z. Marczenco and M. Balcerzak. *Separation, Preconcentration and Spectrophotometry in Inorganic Analysis*. Elsevier Science B.V., 2000.

[57] S. Svanberg. *Atomic and molecular spectroscopy: basic aspects and practical applications*. Springer, 2003.

[58] J. Raty, K.-E. Peiponen, and T. Asakura. *UV-Visible Reflection Spectroscopy of Liquids*. Springer, 2004.

[59] Coefficient of determination. `http://www.public.iastate.edu/~alicia/stat328/Regression%20inference-part3.pdf`, January 2012.

[60] Ceramis officeal website. `www.ceramis.com`, November 2011.

[61] Keithley. *Series 2400 SourceMeter*, revision j edition.

[62] Keithley. *Series 2600A System SourceMeter*, revision d edition.

[63] Hsin-Hsuan Huang, Sheng-Yuan Chu, Po-Ching Kao, and Yung-Chen Chen. High efficiency white organic light emitting diodes using rubrene doped n,n′-bis-(1-naphthyl)-n,n′-diphenyl-1,1′-biphenyl-4,4′-diamine as an emitting layer. *Thin Solid Films*, 516(16):5669–5672, 2008.

[64] M.S. Xu, J.B. Xu, and J. An. Visualization of thermally activated morphology evolution of n, n -di(naphthalene-1-yl)- n, n -diphthalbenzidine films on ito/copper phthalocyanine underlying layer. *Applied Physics A*, 81:1151–1156, 2005.

[65] M.S. Xu and J.B. Xu. Visualization of thermally-activated degradation pathways of tris(8-hydroxyquinoline) aluminum thin films for electroluminescence application. *Thin Solid Films*, 491:317 – 322, 2005.

[66] Jan Wurm. *Glass Structures: Design and Construction of Self-Supporting Skins*. Verlag AG, 2007.

[67] Material properties of pet. `http://www.matbase.com/material/polymers/reinforced/pet-gf30/properties`, February 2012.

[68] O. Geschke, H. Klank, and P. Tellemann. *Microsystem Engineering of Lab-On-A-Chip Devices*. Wiley-VCH, 2004.

[69] S.K. Saha, Y.K. Su, and F.S. Juang. Temperature dependence of electroluminescence in a tris-(8-hydroxy) quinoline aluminum (alq3) light emitting diode. *IEEE Journal of Quantum Electronics*, 37(6):807–812, 2001.

[70] Sheng S. Li. *Semiconductor Physical Electronics*. Springer, 2006.